



HAL
open science

Thermal evolution of the intracratonic Paris Basin: insights from 3D basin modelling

Martina Torelli, Renaud Traby, Vanessa Télès, Mathieu Ducros

► To cite this version:

Martina Torelli, Renaud Traby, Vanessa Télès, Mathieu Ducros. Thermal evolution of the intracratonic Paris Basin: insights from 3D basin modelling. *Marine and Petroleum Geology*, 2020, 119, pp.104487. 10.1016/j.marpetgeo.2020.104487 . hal-02913102

HAL Id: hal-02913102

<https://ifp.hal.science/hal-02913102>

Submitted on 7 Aug 2020

HAL is a multi-disciplinary open access archive for the deposit and dissemination of scientific research documents, whether they are published or not. The documents may come from teaching and research institutions in France or abroad, or from public or private research centers.

L'archive ouverte pluridisciplinaire **HAL**, est destinée au dépôt et à la diffusion de documents scientifiques de niveau recherche, publiés ou non, émanant des établissements d'enseignement et de recherche français ou étrangers, des laboratoires publics ou privés.

1 **Thermal evolution of the intracratonic Paris Basin: insights from**
2 **3D basin modelling**

3 Martina Torelli¹, Renaud Traby¹, Vanessa Teles¹ and Mathieu Ducros^{1,2}

4 ¹ *IFP Energies nouvelles, 1-4 avenue de Bois-Préau, 92852 Rueil-Malmaison, France*

5 ² *Now in C6+ Consultoria e Treinamento em Informática Ltda., Rio de Janeiro, Brazil*

6 Corresponding author.

7 Email address: martina.torelli@ifpen.fr (M. Torelli)

8

9

Abstract

10 The thermal evolution of the Paris Basin (PB) has been widely studied using 1D, 2D and, more rarely,
11 3D thermal models. It is well documented that the PB experienced higher temperatures in the past
12 compared to what is currently observed. However, a quantitative analysis of the main processes and
13 parameters that affect the temperature distribution, at the basin scale and over time, is still not
14 available. In this study, through basin modeling which accounts for the main processes of the thermal
15 evolution of sedimentary basins, we analyze and quantify the role of the different geological
16 mechanisms by discriminating the causes of abnormal temperatures during the Late Mesozoic. This is
17 done with a 3D basin model built from base Moho to present-day topography using the TemisFlow®
18 basin modelling software. The model includes thermal processes within an evolving upper crust
19 defined by three main structural domains. Each crustal sector presents radiogenic heat production,
20 conductivity and thickness values which are used as input parameters to reproduce the paleo- and
21 present-day basal heat flow variations observed in the basin. The model calculates heat flow through
22 time in both, crust and sedimentary column where the crust is coupled with the geological evolution of
23 the basin. This approach allows estimating the eroded thickness during the main Tertiary uplift event
24 and therefore the maximum temperature in the Late Cretaceous. The model is constrained by different
25 types of paleo-thermo-chronometers and by 52 wells that are regionally distributed over the entire

26 basin, resulting in a new regional thermal history of the PB. The amount of missing section in the
27 Cretaceous chalk which mainly affected the eastern part of the basin is increased by up to 500m
28 compared with previous studies and constitutes the key controlling factor of the temperature evolution.
29 This new regional thermal history of the Paris Basin may be important for further analysis of the HC
30 generation from the Lower Jurassic Toarcian source-rock and bring new insights into the geothermal
31 potential of the basin.

32 **1. Introduction**

33 The Paris Basin has been widely studied over the past decades for its petroleum potential [Tissot, et al.
34 1987; Wendebourg and Lamiroux 2002; Delmas et al., 2002] and for geothermal energy studies [Lopez et
35 al. 2010; Réveillère et al. 2013; Boissavy and Grière 2014]. Understanding its present-day and paleo-
36 temperatures is crucial to assess both the location of sweet-spots of maturity and its hydrothermal potential.
37 Many evidences indicate that the basin experienced much higher temperatures in the past than today
38 [Guilhaumou and Gaulier 1991; Guilhaumou 1993; Demars and Pagel 1994; Gaulier and Burrus 1994;
39 Uriarte 1997; Gonçalves et al. 2004, 2010]. Most of the previous studies tried to integrate various kinds of
40 paleo-thermometers to constrain as much as possible the thermal evolution during the Cretaceous, but the
41 basin thermal history remains uncertain. Demars and Pagel [1994] investigated paleo-temperatures from
42 fluid inclusions from 4 boreholes located in the centre of the basin. Their results highlighted a difference of
43 more than 40°C between the present-day and the past. Based on homogenization temperatures, they
44 reached the conclusion that both an important burial and a major erosion event affected the basin during the
45 late Cretaceous time. However, they did not estimate the amount of the eroded thickness. Uriarte [1997]
46 and later Blaise et al. [2014] integrated a whole set of thermal indicators (fluid inclusions, apatite fission
47 tracks, clay diagenesis, biomarkers) to more accurately estimate past temperatures and analyze the possible
48 effect of the Cretaceous chalk sediments (eroded thickness and thermal conductivity) and of the thermal
49 boundaries (surface temperature and basal heat flow). However, their studies were limited to 1D models
50 which are difficult to apply at basin scale. Gaulier and Burrus [1994], with 2D models, and Gonçalves et al.
51 [2004, 2010], with a 3D model, discussed basin scale mechanisms and proposed a regional estimation of

52 eroded chalk thickness. They concluded that an effort should be dedicated to better constrain these
53 estimates. In fact they used constant basal heat flow (in time) as bottom boundary condition which does
54 consider neither the thermal evolution of the basin (like the effects of sedimentation and erosion on the
55 basal heat flow) nor the regional geological differences within the PB (thermal subsidence, variation of
56 basement properties, crustal and mantle depth variations). Le Solleuz et al. [2004] and Bonté et al. [2010]
57 worked on the lithospheric part of the basin to better estimate its basal heat flow and make the link with the
58 sedimentary overburden. However, none of their work aimed at estimating thermal history as they are
59 focused either on the geometrical reconstruction of the crust or on the temperature distribution at present-
60 day only [Bonté et al. 2010]. Despite of all these studies, major uncertainties remain about the maximum
61 temperature reached by the sediments and the temperature evolution over time. What is lacking is a
62 comprehensive study that integrates the full set of thermal data in a 3D geological model that accounts for
63 the thermal mechanisms in both sediments and basement and reconstructs the past thermal regime of the
64 Paris Basin which in turn can be used for petroleum and geothermal applications.

65

66 In our study, a 3D numerical model of the Paris Basin is constructed that accounts for the history of
67 sediment deposition and erosion, of basal heat flow, of surface temperature and of thermal properties of the
68 sedimentary fill. Basement lithology is characterized by lateral compositional heterogeneities [Autran et al.
69 1986; Martelet et al. 2013] which can impact the thermal state of a basin [Welte et al. 1997; Allen and
70 Allen 2013; Dembicki 2016; Souche et al. 2017] and therefore we also included in the model an underlying
71 lithosphere which consists of upper crust, lower crust and upper mantle and whose base is given by the
72 Lithosphere-Asthenosphere Boundary (LAB). Basal heat flow through time depends on the geometry of the
73 lithosphere including any radiogenic heat production from the upper crust and on the transient effects of
74 deposition, compaction or erosion of overlying sediments. Lithosphere geometry is assumed to be constant
75 in time and therefore heat flow varies during geological times mainly as a function of (1) thermal
76 conductivity of sediments which itself depends on facies heterogeneities, porosity and temperature, and of
77 (2) sedimentation and erosion rates. By coupling a lithospheric model with sedimentation, the total amount
78 of eroded thickness during the Cretaceous and the thermal evolution of the basin through time is better
79 estimated while also calibrated to different published thermal data [Gable 1978, 1979, 1988, 1989; Gable et

80 al. 1982; Guilhaumou 1993; Uriarte 1997; Mangenot et al. 2017, 2018]. The present-day thermal state is
81 calibrated using temperature data [Gable 1978, 1979, 1988, 1989, Gable et al. 1982] from 52 wells
82 regionally distributed in the basin. The paleo-thermal regime is calibrated integrating different kinds of
83 paleo-thermometers, such as vitrinite reflectance [Uriarte 1997], fluid inclusions [Guilhaumou 1993] and
84 temperature from clumped isotopes [Mangenot et al. 2017; 2018]. This reduces uncertainties related to any
85 single data type such as vitrinite reflectance which measures the maturity at the highest temperature to
86 which the rock was exposed [Jones and Edison 1979; Oberlin et al., 1980]. Surface temperature variations
87 through time [van Hinsbergen et al. 2015] are applied as top boundary condition of our model. Since
88 groundwater flow at regional scale may induce a heating or a cooling of the system [Allen and Allen 2013;
89 Dentzer et al., 2016] we also analyzed the impact of the fluid circulation which could play an important
90 role in the temperature distribution [Dembicki 2016].

91 Along with the geological information of the sedimentary history of the Paris Basin and a full description
92 of the lithosphere from the LAB to the top basement, we used different types of paleo-thermometers and
93 obtained a well constrained 3D model of the thermal evolution of the Paris Basin which allows us to
94 discuss and quantify the impact of the different mechanisms controlling the thermal evolution of the basin.

95 **2. Geological setting**

96 **2.1. Geodynamic evolution**

97 The Paris Basin is a Meso-Cenozoic intracontinental sedimentary basin that is characterized at the surface
98 by a pattern of concentric sediment outcrops [Megnien 1980; Brunet and Le Pichon 1982; Curnelle and
99 Dubois 1986; Delmas et al. 2002; Beccaletto et al. 2011; Teles et al. 2014] (Fig.1). The Meso-Cenozoic
100 section reaches a maximum thickness of 3 km in the central part of the basin. The basin is bounded by four
101 crystalline massifs (Fig.1), corresponding to the outcropping basement: the Ardennes (NE), the Vosges (E),
102 the Massif Central (S) and the Armorican Massif (W) [Guillocheau et al., 2000 Delmas et al. 2002;
103 Beccaletto et al. 2011; Teles et al. 2014]. During the Paleozoic, the area was affected mainly by the
104 Caledonian and Hercynian orogenies. During a post-orogenic rifting event, caused by the Hercynian
105 massive collapse, strong fault activity led to a rapid subsidence in some specific regions (e.g. Saar-Lorraine

106 basin and Contres-Brecy basin). These small and deep Permo-Carboniferous basins were filled-in with
107 continental coal-bearing sediments [Perrodon and Zabek 1990; Delmas et al. 2002]. This phase strongly
108 impacted the basement structure [Autran et al. 1980] resulting in a complex structure of the upper crust
109 heritage of different Variscan domains [Guillocheau et al. 2015]: the central-Armorican zone and
110 Cadomian block in the western part, the Liguro-Arverne and Morvan-Vosges domains in the south-eastern
111 area (or internal domain), the Saxo-Thuringian zone in the west and in the central part of the basin and the
112 Rheno-Hercynian zone in the northern part [Beccaletto et al. 2011] (Fig. 1). The lateral contact between the
113 different basement domains results in a variable basal heat flow which is higher in the south-western part of
114 the basin compared to the north-eastern area. The Hercynian collapse also led to the creation of major
115 faults: the northwest-east Bray-Vittel fault, the northwest-south Seine-Sennely fault, the north-south Saint
116 Martin de Bossenay and the northeast-southwest Metz fault [Perrodon and Zabek 1990; Delmas et al.
117 2002]. These faults are the lateral boundaries of the crustal domains (Fig.1) that affect the sedimentary
118 filling of the basin up to the present day.

119 After the Permian phase, the basin experienced several episodes of thermal subsidence acceleration-
120 deceleration during the early Triassic [Prijac et al. 2000] due to major geodynamic events linked to the
121 western European plate movements, such as the opening and closing of the Tethys sea and the opening of
122 the Atlantic Ocean [Brunet and Le Pichon 1982; Guillocheau 1991; Loup and Wildi 1994; Prijac et al.
123 2000]. These events were recorded in the Mesozoic sediments with several transgression-regression cycles,
124 detailed in Guillocheau et al. [2015], resulting in a slightly asymmetric geometry of the basin due to
125 different erosion events which affected mainly the eastern edge during the Meso-Cenozoic period
126 [Perrodon, and Zabek 1990] (Fig.1).

127 The sedimentary cover described in our model includes the entire section from the Permo-Carboniferous to
128 the Neogene, since the sedimentary infill plays a crucial role on the heat flow distribution in the basin. The
129 model does not account for the Paleozoic rifting phase as the interest of this study is more related to the
130 thermal evolution of the basin during Mesozoic and Cenozoic times.

131 **2.2. Lithostratigraphic evolution**

132 During its early stages the Paris Basin constituted the western border of the German Basin, characterized
133 by deposition of sediments prograding from east to west [Megnien 1980; Ziegler 1980; Perrodon, and

134 Zabek, 1990]. The three fundamental Triassic units consist of different types of deposits. The
135 Buntsandstein sandstones and conglomerates are typical of alluvial plain deposits. The Muschelkalk
136 formation marked the transition to an open sea environment with the deposition of marls, carbonates and
137 evaporitic sediments. The Keuper formation mainly consists of sandstone with black shale intercalations
138 deposited during a regressive trend which marked the transition from littoral facies to coastal/alluvial plain
139 sediments [Guillocheau et al. 2015].

140 During the Lower Jurassic, the Paris Basin experienced an increase in its subsidence rate, evolving into a
141 more extensive basin. From this time the sedimentation was characterized by deposition of marls and
142 organic matter rich-shales representing the three main source rocks of the basin: the
143 Hettangian/Sinemurian, the Pliensbachian and the Toarcian (Schistes Carton Formation) [Guillocheau et al.
144 2015]. The beginning of the Dogger marked the transition to a carbonate platform environment [Purser
145 1975; Curnelle and Dubois 1986] with episodes of drowning indicated by clay-rich deposits. The basin was
146 characterized by regressive sequences until the Middle Oxfordian and the depositional environment
147 gradually returned to carbonate sedimentation. During the Tithonian, the Paris Basin underwent a first
148 important regression period of accommodation space removal followed by detrital deposition during early
149 Cretaceous. From the Aptian time, an eustatic sea-level rise led to the accumulation of a thick chalk layer
150 in the entire basin. The boundary between the Mesozoic and Cenozoic is marked by the Laramide erosional
151 event. The exact eroded thickness of the chalk deposit is not clear but previous modelling results [Uriarte
152 1997; Gonçalvès et al. 2010], constrained by geochemical datasets [Demars and Pagel 1994; Uriarte 1997],
153 suggested that more than 300 meters were eroded in the central part of the basin and more than 500 meters
154 were eroded in the edges of the basin. Since this time, the basin has been under exposure and erosion with
155 the subsequent exhumation of the underlying sediments [Ziegler 1988; Blaise et al. 2014]. Considering that
156 erosion events are particularly important in the thermal evolution of this basin, this point will be
157 specifically addressed and discussed in the results and discussion sections.

158 **3. Data set**

159 **3.1. Temperature data**

160 Temperature data from 52 wells are available in BRGM (Bureau de Recherches Géologiques et Minières)
161 and IFPEN (IFP Énergies nouvelles) reports [Gable 1978 , 1988, 1989 ; Gable et al. 1982]. The data include
162 different kinds of present-day temperature measurements (Fig.2):

- 163 - 14 of the wells from the BRGM reports [Gable et al. 1982; 1988, 1989] provide temperature logs
164 registered every 0.16 m from the top to the bottom of the wells. These measurements were carried
165 out after reaching the thermal equilibrium state, and thus they give an accurate measure of the
166 present-day thermal state in the basin.
- 167 - Corrected Bottom Hole Temperatures (BHT) are available for 28 of the wells, for which the
168 uncertainty was estimated to be $\pm 4^{\circ}\text{C}$ [Gable 1988].
- 169 - Uncorrected BHT are also available for 10 wells [Monnet, 2006]. According to Deming [1989],
170 BHT value correction can lead to an increase of more than 10% of the observed values in a well.
171 Since no information was available on how these measurements were performed, it was decided first
172 to correct these temperatures by adding 10% and to assume a $\pm 10\%$ range of uncertainty. These
173 BHT measurements are of lower reliability but are the only ones to bring a better regional coverage
174 for the thermal model calibration along the border of the basin, which is an important contribution
175 for the regional estimation of basement properties and consequently of the eroded thickness.

176 Present-day crustal heat flow varies laterally in the basin as the result of basement heterogeneities [Gaulier
177 and Burrus, 1994; Lucazeau and Vasseur 1989] which lead to an important geothermal gradient variability in
178 the entire basin. Figure 3 shows the comparison between measured geothermal gradients from wells located
179 in the southwestern part of the basin (e.g. Sennely and Puiset) and those located in the center and north-
180 eastern area (e.g. Montmirail and Morhange). Thermal gradient is much higher ($40^{\circ}\text{C}/\text{km}$) in the south-
181 western part of the basin than in the northern part ($30^{\circ}\text{C}/\text{km}$). For this reason, it was important to include
182 wells that are located farther from the depocenter since they allowed the calibration of the thermal history of
183 the entire basin area (Fig.2).

184 **3.2. Paleo-thermal regime**

185 The paleo-thermal regime was calibrated using vitrinite reflectance data [Uriarte 1997], trapped temperatures
186 from fluid inclusions [Guilhaumou 1993] and clumped isotopes (Δ_{47}) [Mangenot et al. 2017, 2018] (Fig.4).

187 Vitrinite reflectance measurements are one of the most common parameters used to calibrate the thermal
188 history of a basin. The vitrinite reflectance data are taken from Uriarte [1997], who divided them into two
189 main categories: measured on coals and measured on dispersed organic matter. Dispersed vitrinite are less
190 reliable since they can be related to reworked material. We calibrated the paleo-thermal regime with the
191 more reliable measurements made on coals. However, as vitrinite reflectance evolves following a kinetic
192 law which is function of time and temperature [Sweeney and Burnham 1990], it is not possible to directly
193 estimate the age of the maximum temperature reached by the sediments.

194 In contrast, the temperatures interpreted from fluid inclusions [Guilhaumou 1993] give the temperature of
195 the fluids when they were trapped during the crystallization of the cements. Thus, the sediment deposition
196 age may be correlated with the trapping temperature estimated from fluid inclusions but remains relatively
197 uncertain. The temperatures estimated by Guilhaumou [1993] and Demars and Pagel [1994] were
198 determined from samples hosted in diagenetic cements of main source and reservoir rocks of the Paris
199 Basin.

200 Clumped isotopes (Δ_{47}) data [Mangenot et al. 2017] combined with U/Pb chronometric measurements
201 [Mangenot et al., 2018] is a very recent technique which relates measures of paleo-temperatures to their
202 age. This new technique has been analyzed, calibrated and tested for different inorganic and biogenic
203 carbonates in the 0°-350°C temperature field range [Ghosh et al. 2006; Dennis and Schrag 2010; Kele et al.
204 2015; Bonifacie et al. 2017; Mangenot et al. 2017]. The link between the temperature estimated from
205 clumped isotopes and the age determined by the U/Pb chronometers can produce a time-temperature
206 evolution path for each analyzed sample [Mangenot et al., 2018]. Mangenot et al. [2018] estimated paleo-
207 temperature and their correlated ages for carbonate samples of the main reservoir rocks.

208 **4. Basin modelling**

209 **4.1. Sedimentary model**

210 An initial model was built with 12 interpreted horizons constructed from outcrops, wells and structural
211 maps based on the work of Teles et al. [2014]. Based on this initial model, we built an extended 3D model
212 in the TemisFlow® basin modelling software, ranging from the LAB to the surface. The model grid is
213 composed of around 3.5 M cells with a horizontal resolution of 2x2 km². A total of 40 geological events is
214 represented (Tab.1): 29 depositional events, 7 erosion events, 3 erosion and deposition events (erosion on
215 the eastern edge during sediment deposition in the central part of the basin) and 1 hiatus. The extension of
216 the investigated area is approximatively 200,000 km². The thermal simulation was performed using a fully
217 coupled lithosphere/sediment for the entire duration of the basin evolution of 330.0 My. The compaction
218 processes are accounted for using the approach of Schneider et al. [1996]. Thermal parameters of
219 sedimentary rocks are given in Table 2. Decompression reconstructs the evolution of the basin geometry in
220 the geological past. A forward simulation of the basin evolution is then performed solving for a coupled
221 pressure-temperature system with Darcy's equation for fluid flow in sediments, and the heat flow equation
222 for temperature in basement and sediments.

223 In the model, each layer is described by a depth map and a lithology map. Seven main erosional events are
224 taken into account (Tab. 1) [Delmas et al., 2002; Guillocheau et al. 2015]. Since Gonçalves [2002, 2003]
225 showed that topography evolution strongly impacts groundwater flow, sixteen paleo-bathymetry maps are
226 used to better constrain the basin topography and flow history, which also impacts the evolution of the
227 sediment bulk thermal conductivity as porosity and effective stress are coupled. Four paleo-bathymetries
228 were digitized from Gonçalves [2002] for the Tithonian, Aptian, Cenomanian and top-Maastrichtian ages.
229 The remaining 12 paleo-bathymetry maps were constructed based on facies distribution and depositional
230 environments (Tab. 1). Since the beginning of the Tertiary, the paleo-bathymetry is assumed to be constant.
231 The final 3D model of the Paris Basin, from the Permo-Carboniferous basins until the Cenozoic cover, is
232 shown in Figure 5.

233

234 **Lithospheric model**

235 A full description of the lithosphere is included in our model which accounts for the thermal conductivity
236 and radiogenic heat production of the crust. This allows to compute the heat flow entering at the base of the
237 sedimentary column instead of imposing it, as in Gaulier and Burrus [1994], Uriarte [1997] or Gonçalves et
238 al. [2010].

239 The basement structure beneath the Paris Basin is poorly known but several information are available in the
240 literature [Weber 1973; Debeglia 1977; Megnien 1980; Autran et al. 1986; Lucazeau and Vasseur 1989;
241 Demongodin et al. 1991; Gaulier and Burrus 1994; Delmas et al. 2002; Beccaletto et al. 2011; Martelet et
242 al. 2013]. Those works suggested that the lithosphere is characterized by heterogeneities in terms of
243 thickness and mineralogical composition as the result of lateral changes between different basement
244 domains that are controlled by the main faults (Fig. 1) [Autran et al. 1986; Delmas et al. 2002; Beccaletto
245 et al. 2011; Martelet et al. 2013]. These faults (Bray-Vittel and Seine-Sennely faults) also explain the
246 observed thermal gradient variations over the entire basin which was used to identify and map three main
247 upper-crust domains as shown in Figure 3.

248 The main basement deformations occurred during the Paleozoic but during the Triassic, the tectonic
249 movements were mostly due to thermal subsidence after a rifting phase that affected mainly the western
250 part of the basin [Brunet and Le Pichon 1982; Guillocheau 1991; Prijac et al. 2000]. Since most
251 deformations occurred during the Permo-Carboniferous age with localized effects, the crustal model was
252 constructed using the assumption that the lithosphere thickness is unchanged during the Meso-Cenozoic
253 [Gaulier and Burrus 1994; Prijac et al. 2000]. The heat flow at the base of the sedimentary column is
254 therefore the result of basement thickness, composition and radiogenic heat production [Debeglia 1977;
255 Autran et al. 1986; Gaulier and Burrus 1994; Martelet et al. 2013] as well as transient effects of
256 sedimentation and erosion.

257 The base of the model is defined by the LAB, adapted from Tesauro et al. [2009] which represents the
258 bottom thermal boundary condition (at 1333°C). The transition between the upper mantle and the lower
259 crust corresponds to the MOHO discontinuity taken from Bourgeois et al., [2007]. The difference between
260 the LAB and the MOHO represents the mantle lithosphere thickness. Its average value is around 100 km, in
261 accordance with other data published by Panza et al. [1980]. The thickness distribution between the upper
262 and the lower crust is not described in literature. Starting from the assumption that the commonly admitted

263 thickness for continental upper crust is 20 km and 12 km for the lower crust [Rudnick and Fountain 1995a],
264 a thickness ratio of 0.6 has been used.

265 **4.2. Surface boundary conditions**

266 The upper thermal boundary condition is applied to the surface topography as an imposed temperature over
267 time. In a marine environment, it is important to correct surface temperatures in accordance with the paleo-
268 bathymetry. Indeed, temperatures at the sea-bottom are usually much cooler than the temperatures in
269 onshore environments at the same latitude [Dembicki 2016]. Surface temperatures are defined from 330
270 Ma to Present-day, according to the *Paleo-latitude Calculator for Paleoclimate Studies* [van Hinsbergen et
271 al. 2015 and references therein]. The temperature estimated for each geological time step (0.1 My) is
272 imposed as a constant value in the entire basin (Fig. 6). This reconstruction showed that the basin was
273 under tropical conditions during its early ages. Then, from the last 20 My, the surface temperature
274 progressively decreased to the current temperate climate.

275 **5. Results**

276 **5.1. Present-day Temperatures**

277 The calibration of the thermal properties of the lithosphere allowed us to match observed temperatures.
278 Since there are differences between the main lithospheric regions of the basin [Weber 1973; Megnien 1980;
279 Lucazeau and Vasseur 1989], the upper crust was defined with three regions with different thermal
280 properties (Tab. 3). Each region is characterized by a radiogenic heat production calibrated on temperatures
281 at wells. In the central and southern part of the basin, the upper crust is characterized by a mean thickness
282 of 19 km and a RHP of $3.7 \mu\text{W}/\text{m}^3$. The western part presents an average thickness of 26 km and an RHP
283 of $4.0 \mu\text{W}/\text{m}^3$ (Duwiquet et al. 2019). The eastern part is characterized by an average thickness of 22 km
284 and a RHP of $3.4 \mu\text{W}/\text{m}^3$. The lower crust was assumed to be laterally homogeneous with a constant RHP
285 of $0.4 \mu\text{W}/\text{m}^3$ [Rudnick and Fountain 1995; Le Solleuz et al. 2004].

286 In order to define the thermal state of the entire area, we used 52 regionally distributed wells of which six
287 are presented in Figure 7 coming from the BRGM report [Gable 1978]. Similar good fits between
288 simulated and measured temperatures were obtained for the other wells used in the calibration process.

289 Within the Liassic and the chalk intervals, the thermal gradient is slightly higher than in other formations.
290 This effect, already described in Gaulier and Burrus [1994], is due to the lower conductivity of the chalk
291 and the Liassic organic matter rich-shale.

292 **5.2. Deposition and erosion of the chalk**

293 The following scenario for the evolution of the chalk deposit during the Upper Cretaceous calibrates the full
294 set of thermal data. A first sedimentation period lasts 11.5 My during which between 700 and 1000 meters of
295 chalk were deposited with an average sedimentation rate of up to 78 m/My, followed by a 20 My hiatus (Fig.
296 8a). A large part of this chalk was removed during the Upper Cretaceous erosional event (Fig. 8b). Erosion
297 ranges from up to 700 m in the SE wedge of the basin, to around 600 m in the center of the basin. In our
298 model, erosion stopped at 66 Ma in the center of the basin, corresponding to the beginning of deposition of
299 the Paleogene sediments, but erosion continues to occur on the margins of the basin until 47.8 Ma (Fig.8c,
300 8d). The final estimated missing section is shown in Figure 9.

301 **5.3. Paleo-Temperatures**

302 **5.3.1. Vitrinite reflectance**

303 Figure 10 shows the calibration results for six wells located in the southern and central parts of the Paris
304 Basin. The measured vitrinite reflectance values range from 0.39% in the shallow layers to 0.69% in deeper
305 layers. The present-day thermal maturity of the three Liassic source rocks (Hettangian/Sinemurian,
306 Pliensbachian and Toarcian Schistes Carton) is shown in Figure 11. These vitrinite data indicate the
307 beginning of the oil window (0.6 - 0.8 %Ro) for the three source rocks, with higher maturity values for the
308 Hettangian/Sinemurian layer (0.8 – 1 %Ro) in the deeper part of the basin.

309 **5.3.2. Fluid inclusions**

310 The modeled burial history has been compared to the burial analysis performed by Uriarte [1997] and to
311 the temperatures derived from fluid inclusions [Guilhaumou 1993]. As shown in Figure 12, for both the
312 Dogger and the Keuper formations, the modeled temperatures through time for Ambreville well are similar
313 to values obtained by Uriarte [1997] with small differences ($\pm 4^{\circ}\text{C}$). They may be related to a different
314 timing between the model proposed by Uriarte [1997] and our model. This is confirmed by the large

315 difference of temperatures at a given age but a small difference of age for a given temperature. The
316 comparison between our model and the models proposed by Uriarte [1997] and Guilhaumou [1993]
317 highlights also the fact that the sediments reached higher temperatures during the Upper Cretaceous in the
318 Keuper formation (125/130°C) and within the Dogger (90/95°C). Since Guilhaumou [1993] did not
319 perform the pressure correction necessary to constrain the timing of mineral precipitation [Roedder 1984;
320 Guilhaumou 1993], there might be an important uncertainty on the cementation age but not on the trapping
321 temperature derived from fluid inclusions. Therefore, more attention is paid to temperatures than to timing.
322 Similar paleo-temperatures were determined by Gonçalves et al. [2010] from fluid inclusions in the Keuper
323 formation, with an average value of 102/140°C (ΔT of 17/44°C) and in the Dogger layer with 68/88°C (ΔT
324 values of 0/18°C).

325 **5.3.3. *Clumped Isotopes***

326 The Paris Basin thermal model has also been compared to the temperatures estimated by clumped isotopes
327 thermo-chronometers (Δ_{47} /U-Pb) [Mangenot et al. 2017, 2018]. The paleo-temperatures and timing were
328 determined on samples from the Dogger formation in three wells located mostly in the central part of the
329 basin: Baulne-en-Brie, Rigny-la-Nonneuse and Fossoy. Figure 13 compares the simulated temperatures and
330 the estimated paleo-temperatures/time derived from clumped isotopes (Δ_{47}) and U/Pb data. The Dogger
331 formation, sampled in the Baulne-en-Brie well, reached a temperature of $49 \pm 5^\circ\text{C}$ during the Upper
332 Jurassic. It is followed by a temperature increase during the Lower Cretaceous, reaching approximately 66
333 $\pm 5^\circ\text{C}$. The temperature estimated in the Rigny-la-Nonneuse well is lower during the Upper Jurassic,
334 reaching around $31 \pm 6^\circ\text{C}$. It is followed by a peak of around $78 \pm 7^\circ\text{C}$ during the Upper Cretaceous and a
335 progressive cooling ($70 \pm 7^\circ\text{C}$) until the Eocene. The temperature estimated from clumped isotopes for
336 Fossoy is the highest, reaching approximately $88 \pm 7^\circ\text{C}$ during the Cretaceous ($107 \pm 13\text{My}$). The modeled
337 time/temperatures histories are in accordance with those estimated from clumped isotopes and U/Pb data in
338 all the wells except for Fossoy well where the maximum temperature is reached at 90 My.

339 **5.4. Heat flow map at the base of the sediments**

340 Figure 14 shows present-day modeled heat flow ranging from 65 to 85 mW/m². The western region (AD
341 domain in Figure 14) has a mean heat flow of 80 mW/m². It slightly decreases towards to the northeastern

342 area (ID domain in Figure 14) with an average value of 70 mW/m^2 . The RHT/STZ domain (Figure 14)
343 which corresponds to the central area of the basin, has the lowest heat flow with a mean of 67 mW/m^2 . The
344 location of the three heat flow domains from the warmest area to the coldest is related to a large part to the
345 structure of the upper crust. The warmer area is located just above the upper crust defined by a high RHP.
346 However, the heat flow results also show the impact of the sedimentary cover on the thermal state of the
347 basin, justifying a coupled thermal modeling approach. The coldest parts of the basin correspond to the
348 central area where the basin has the thickest sedimentary cover, and to the Permo-Carboniferous rift basins
349 (e.g. Saar-Lorraine basin and Contres-Brecy basin) where the sedimentary cover exceeds 3 km.

350 **6. Discussion**

351 **6.1. Heat flow map**

352 The present-day temperatures of the 52 wells distributed over the entire area allowed us to identify the
353 boundary of the three different thermal domains of the upper crust. The contact between the three domains
354 follows the main faults structuring the basement (Bray-Vittel fault, Seine-Sennely fault and Saint Martin de
355 Bossenay fault) (Fig.1) that are inherited from the complex deformations at the junction between major
356 regions of the Variscan collision belt [Martelet et al. 2013]. First Autran et al. [1986] and then Martelet et al.
357 [2013] tried to reconstruct the geometry of the basement beneath the Paris Basin based on magnetic and
358 gravity data. Both groups of authors agreed that magnetic and gravity anomalies are linked to mineralogical
359 heterogeneities such as lateral variation of igneous rocks (intrusive and extrusive) characterized by different
360 density values. Thermal parameters from these different upper-crust domains, such as RHP and
361 conductivities were used as key controlling parameters to fit observed temperatures.

362 In a previous work, Lucazeau and Vasseur [1989] published a heat flow map of France, built on local heat
363 flow values from several thermal logs in shallow boreholes (with depths ranging from 100 m to 1000 m).
364 Their average heat flow was estimated between 60 and 70 mW/m^2 , with occasional higher values of 100 -
365 110 mW/m^2 (e. g. for the Rhine Graben or the Massif Central) and occasional lower values of 40 mW/m^2
366 (western part), but also local anomalies that reached 150 mW/m^2 in the same area. This approach is highly
367 dependent on the quality of the temperature correction which may result in large uncertainties of the true

368 temperatures. Also, it does not take into account the temperature variations that are strongly correlated to
369 the sediment thermal conductivities of a 3km-thick sedimentary column. According to Gonçalves et al.
370 [2010], the heat flow values which range from 60 to 100 mW/m², are regionally variable due to basement
371 heterogeneities which however is not taken into account as basal heat flow maps are used. In our work, we
372 obtain the same order of magnitude but the heat flow map of the Paris Basin at present-day is the result of
373 the combined effects of basement and sedimentary cover. As shown in Figure 15, the resulting basal heat
374 flow appears to vary significantly both in time and in space. The description of the lithosphere
375 configuration was crucial to reproduce the effect of temperature variations in the basin already described by
376 previous authors [Lucazeau and Vasseur 1989; Demongodin et al. 1991; Gonçalves et al. 2010; Martelet et
377 al. 2013].

378 **6.2. Erosions**

379 One of the challenges in basin modelling is to estimate erosion events and heat flow together as they
380 compensate each other. Using a lithospheric model coupled with sedimentation allows to better constrain
381 the eroded thickness which is done in two steps: first by fixing/calibrating the crustal properties (mainly
382 RHP) using temperature data (which mostly depend on RHP and on depth) and then using paleo-
383 temperatures and paleo-thermometers to estimate the eroded thickness.

384 In the Paris Basin, erosion events played a decisive role on the burial history and consequently on the
385 maturity reached by any organic-rich sedimentary layer. The Upper Cretaceous erosional event (amplitude,
386 timing and rate of erosion) strongly affects the evolution of the thermal history of the Paris Basin. Special
387 attention was therefore given to the description of the Maastrichtian erosion as it is the most recent erosion
388 event which has the most significant impact on the maximum burial of the basin. Demars and Pagel [1994]
389 suggested that an important event affected the basin during the Cretaceous time. Indeed, paleo-
390 temperatures from fluid inclusions show that the basin experienced higher thermal condition during the
391 Cretaceous than today. According to the authors, this effect could not be explained by migration of hot
392 brine fluids since they would only affect the basin at a local scale. Their assumption was that the basin
393 experienced a deep burial event followed by an erosion. However, they did not define average values for
394 the eroded thickness neither did they account for any surface temperature variation.

395 After Demars and Pagel [1994], others studies such as Gaulier and Burrus [1994], Uriarte [1997] and
396 Gonçalves et al. [2010] tried to quantify and to describe the deposition of the chalk sediments during the
397 Upper Cretaceous, using a modelling approach. Gaulier and Burrus [1994] constrained the chalk erosion
398 properties in the eastern part of the basin by thermal modeling of an E-W cross section through the Paris
399 Basin using a few paleo-thermal constraints and a constant basal heat flow. Their model was calibrated
400 with a maximum eroded thickness of 350 meters during the Upper Cretaceous. With such a 2D setting, it is
401 possible to achieve higher temperatures that compensate the erosion effect with an over-estimated heat
402 flow at the base of the model, but it is difficult to accurately infer the amplitude of the erosion. In his 1D
403 thermal models of the southern central part of the Paris Basin, Uriarte [1997] used the same bottom heat
404 flow proposed by Gaulier and Burrus [1994] and increased the chalk eroded thickness during the Upper
405 Cretaceous to a maximum value of 600 m. Similarly, Gonçalves et al. [2010], also with an imposed heat
406 flow at the base of their 3D model that varies in space but not in time, increased the eroded thickness from
407 the initial estimated value of 300 m [Gaulier and Burrus 1994] up to 650 m to reproduce the trapping
408 temperatures measured in fluid inclusions.

409 Due to the low maturity of the source rock ($0.3 - 0.7\%Ro$), the calibration of the vitrinite reflectance data is
410 relatively insensitive to assumptions on the chalk eroded thickness, therefore fluid inclusion and clumped
411 isotope data are crucial. Using such published data [Guilhaumou 1993; Uriarte, 1997; Mangenot et al.,
412 2017; 2018], we propose a new scenario for the erosion event during the Upper Cretaceous. The bottom
413 boundary condition of the sedimentary basin is computed with the lithospheric model and spatially variable
414 RHP (as discussed in the previous section) which prevents arbitrary (user-defined) compensation between
415 basal heat flow and eroded thickness. This new alternative scenario provides a temperature history in good
416 agreement with the temperatures inferred from the clumped isotopes study of Mangenot et al. [2017]. A
417 particular data point is the high temperature value encountered in the Fossoy well (88 ± 7 °C). It was
418 interpreted by Mangenot et al., [2018] as a thermal anomaly probably due to local hydrothermal activity. In
419 this study, all clumped isotopes values measured in 3 different wells have been compared against the
420 temperature computed at the Ambreville well (Fig.3) that was used by Uriarte [1997] for his 1D thermal
421 model. However, these wells are not located in the same area, as they are 40km to more than 90 km away.
422 As shown in Figure 16, the thermal evolution of two wells located in different parts of the basin are quite

423 different (see locations in Fig.1 and Fig.9). The central part of the basin (e.g. Montlevée) underwent a
424 maximum burial of more than 3 km as the result of the chalk deposition during the Upper Cretaceous and it
425 was almost not affected by the erosion event during the Paleocene. At a well located in the eastern part of
426 the basin (e.g. Silvarouvres), sediments experienced a lower burial, around 1.2 km, which lead to different
427 maximum temperatures and maturity conditions. With our geological scenario, all temperature histories are
428 in agreement with the paleo-temperatures estimated in each well from vitrinite data, fluid inclusions and
429 clumped isotopes (Δ_{47}) with a slight shift in age in the Fossoy well (estimated age from U/Pb 107 ± 13 My,
430 modeled age 90 My) (Fig.11). This discrepancy may be the consequence of a local effect such as a faster or
431 earlier deposition of the chalk sediments. Since all available thermal data can be explained with this
432 regional scenario which is geologically consistent with the current knowledge of the basin evolution, it is
433 therefore also reasonable to suggest that the Paris Basin experienced the highest temperature during the
434 Upper Cretaceous caused by an overburden event. This hypothesis of a large scale spatially distributed
435 deposition/erosion event was already proposed by Gonçalvès et al. [2010].

436 We conclude that, at the end of the Cretaceous, the basin experienced its maximum burial due to the
437 deposition of an important chalk section. This age corresponds also to the age of maximum temperature
438 recorded by the sediments which subsequently slowly decreased until the present-day (as showed for the
439 Dogger reservoir in Figure 17). The increase of temperature at the end of the Cretaceous can be explained
440 by two combined/coupled effects: an increase in burial and higher thermal gradients of the sediments below
441 the chalk caused by their lower thermal conductivity [Guilhaumou & Gaulier 1991; Guilhaumou 1993;
442 Gonçalvès et al. 2010]. We neglected any variability of chalk thermal conductivity which may have an
443 impact on the final erosion estimate. The differences of the thermal evolution of each well highlight the
444 importance of a 3D assessment of the geodynamic, stratigraphic and tectonic evolution of the Paris Basin.

445 **6.3. Surface temperature variations**

446 In previous studies [Habicht 1979; Gaulier and Burrus 1994], the mean surface temperature of the Paris
447 Basin was considered constant at 15°C from the Triassic until the Upper Cretaceous. According to these
448 authors, the basin only recorded momentarily higher mean temperatures (reaching 20°C) but it decreased
449 during the Upper Cretaceous and decreased again during the Tertiary down to 5°C at the present day. In our

450 study, the Paris Basin experienced a mean paleo-surface temperature of 20°C until the Cretaceous, with a
451 higher temperature of 25°C recorded during the Lower Triassic and the Upper Cretaceous (Fig. 6). This
452 higher temperature at 85 Ma also contributed to the higher paleo-geothermal gradient. However, this
453 contribution rapidly decreases with depth as surface temperature mostly controls shallow parts of
454 sedimentary basins.

455 In order to determine the surface temperature at the sea/sediment interface, the paleo-bathymetry of the
456 study area through time should be taken into account. In this study however, this correction was not
457 performed. It could slightly reduce past temperatures but should not have any impact on the maximum
458 temperature as we assume that it was recorded during the Upper Cretaceous which corresponds to a
459 depositional hiatus with a transitional setting from marine to continental environment.

460 **5.4. Blanketing effect and the role of the chalk**

461 As showed by Theissen and Rüpke [2009], when the sedimentation rate exceeds 500 m/My it affects the
462 heat flow through the sedimentary column with a transient effect. This effect occurs when cold sediments
463 are being added to the column faster than they can be equilibrated thermally. Consequently, shallow
464 temperatures do not follow a normal thermal gradient but are lower than steady state. When the
465 sedimentation rate decreases, the thermal gradient progressively increases until the system reaches thermal
466 equilibrium.

467 According to our model, the Paris Basin recorded the deposition of 700 to 1000 m of sediments within 11.5
468 My during the Cretaceous interval which corresponds to an average deposition rate of 78 m/My (moderate
469 sedimentation rate according to Theissen and Rüpke [2009]). Rather than from fast sedimentation, the high
470 temperatures estimated for the Paris Basin during the Upper Cretaceous can be explained by the physical
471 properties of the sediments that were deposited at this time. The high porosity of the chalk [Guilhaumou
472 and Gaulier 1991; Guilhaumou 1993; Demars and Pagel 1994] leads to very low thermal conductivity of
473 $1.2 \text{ W m}^{-1} \text{ C}^{-1}$ compared to the average value of sediments of about $3.5 \text{ W m}^{-1} \text{ C}^{-1}$ [Thomas et al. 1973]. The
474 chalk therefore acts as a thermal barrier which prevents heat to reach the shallower part of the basin and
475 results in heat accumulating in the underlying formations.

476 In our model, after the deposition of around 1000 m of chalk over the entire basin, a hiatus of 20 My was
477 assumed. In this case, the thermal barrier induced by the chalk is one of the most important mechanisms to

478 explain the high temperatures reached during the Upper Cretaceous. The Tertiary erosion along with a
479 decrease of the surface temperatures can then explain how the temperature slowly declined from the
480 Cretaceous until present day.

481 **5.5. Fluid hydrodynamics and advection**

482 The Paris Basin is considered an important geothermal resource [Contoux et al. 2013; Boissavy and Grière
483 2014]. In order to investigate the potential impact of water circulation on the Paris Basin thermal evolution
484 by heat transfer through gravity-driven groundwater flow, we compared two simulation results. In the first
485 simulation, both advection and conduction were simulated while, in the second one, advection was
486 deactivated considering only conduction. According to our results, the differences on the thermal regime
487 between the two simulations are negligible both for the temperatures, with differences lower than the
488 uncertainty on the measured temperatures ($< 2^{\circ}\text{C}$), and for the maturity. Therefore, water advection does not
489 appear as one of the major mechanisms controlling the temperature distribution in the basin. However,
490 changes in boundary conditions may affect fluid flow and create transient effects [Jost et al. 2007]. Lavastre
491 et al. [2010] proposed a hydrodynamic model at small scale, mainly located in the central part of the Paris
492 Basin. They determined that the deeper Jurassic aquifers (mainly Oxfordian and Dogger) are characterized
493 by no convective mixing with a late water recharge at 10 ky. The estimated residence time of several 100 ky
494 implies slow water flow transfer with an order of magnitude lower than proposed by Gonçalves et al. [2004]
495 who set the boundary conditions far away from those of the present-day of the basin, with the main discharge
496 areas in the English Channel. Here, we did not try to reproduce the hydrodynamic pattern of the Paris Basin
497 but we do observe that, at the time and space scales of our basin model, water flow does not have a major
498 impact on the temperature distribution over time. This result validates the assumption that subsurface fluid
499 flow is slow enough for the water to be in equilibrium with rock temperature most of the time during the
500 geological evolution of the Paris Basin. This does not mean that water circulation cannot have local effects in
501 areas where the topographic gradient is locally higher [Marty et al. 1993].

502 **7. Conclusions**

503 This study produced a well constrained thermal history of the Paris Basin using several types of thermal
504 data [Gable 1978, 1979, 1982, 1988, 1989; Guilhaumou 1993; Uriarte 1997; Mangenot et al. 2017, 2018]. A
505 3D numerical model provides new insights of the impact of different mechanisms on the thermal evolution
506 of the Paris Basin. The use of a coupled sedimentary-lithospheric model calibrated by a full set of good
507 quality thermal data allowed us to quantify and discriminate the contributions of surface temperature,
508 blanketing effect of the chalk deposits, Tertiary erosion and water flow. The new paleo-thermal constraints,
509 derived from the clumped isotopes (Δ_{47}) technique [Mangenot et al. 2018], show that the basin exhibited
510 higher temperature during the Upper Cretaceous. These data, which have been interpreted as a possible
511 thermal anomaly due to hydrothermal effects [Mangenot et al. 2018], are essential to accurately calibrate the
512 thermal history of the Paris Basin as they give better constrains on the timing than vitrinite reflectance data.
513 These data also allowed us to propose a new scenario for the basin evolution, based on its burial history and
514 thermal rock properties.

515 The higher temperatures registered by the sediments during the Upper Cretaceous age are interpreted as a
516 consequence of an important depositional event. The deposition of a thick chalk layer with a very low
517 thermal conductivity acted as a thermal barrier, keeping the underlying sediment at higher temperatures.
518 This event was of a major importance to fit the available paleo-thermometers such as vitrinite reflectance
519 data, since the entire sedimentary column has been buried at high temperatures for an extended time,
520 allowing the sediments to mature early. During the Maastrichtian which we defined as a depositional hiatus
521 of 20 My, the basin changed from a marine setting to a subaerial environment. The subsequent erosion leads
522 to up to 1000 meters of uplift from Upper Cretaceous to Tertiary, and a decrease of about 10°C of the
523 surface temperature, which caused a strong decrease in the subsurface temperatures until today. Note that
524 these values represent about 500 m of additional erosion compared to previous studies. No significant
525 impact on the thermal regime has been observed in the model due to water flow.

526 The 3D nature of our model, the quality of the calibration and the variety of the constraints improve our
527 understanding of the thermal evolution of the Paris Basin. By constructing a geologically coherent
528 lithospheric model coupled with sedimentation, we can more accurately than before estimate the amplitude
529 of the Maastrichtian erosion at a regional scale while obtaining a good match between modeled and observed

530 temperatures. Such a well-constrained thermal history will help any further analysis of the Lower Jurassic
531 Toarcian source-rock generation history and may bring new insights to the petroleum and geothermal
532 potential of the basin.

533 **Acknowledgement**

534 The authors would like to thank Pascal Houel (IFPEN) for his precious and constructive advices. We would
535 also like to thank Quintijn Clevis and Fausto Mosca for their constructive reviews and for additional
536 comments by Associate Editor Johannes Wendebourg that helped greatly to improve this paper.

537 **8. References**

- 538 ALLEN P.A. AND ALLEN, J.R. 2013. BASIN ANALYSIS: PRINCIPLES AND APPLICATION TO PETROLEUM PLAY ASSESSMENT,
539 THIRD EDITION, WILEY-BLACKWELL, OXFORD, 619PP.
- 540 AUTRAN, A., CASTAING, C., DEBEGLIA, N., GUILLEN, A., AND WEBER, C. 1986. Nouvelles contraintes géophysiques et
541 géodynamiques pour l'interprétation de l'anomalie magnétique du bassin de Paris; hypothèse d'un rift
542 paléozoïque refermé au Carbonifère. *Bulletin de la Société Géologique de France II*, 1, 125–141.
- 543 AUTRAN, A., DEBEGLIA, N., FEYS, R., GREBER, C., AND MEGNIEN, C. 1980. Socle du Bassin. In *Mémoire BRGM*, 17–
544 36.
- 545 BECCALETTO, L., HANOT, F., SERRANO, O., AND MARC, S. 2011. Overview of the subsurface structural pattern of
546 the Paris Basin (France): Insights from the reprocessing and interpretation of regional seismic lines.
547 *Marine and Petroleum Geology*, 28(4), 861-879.
- 548 BLAISE, T., BARBARAND, J., KARS, M., PLOQUIN, F., AUBOURG, C., BRIGAUD, B., CATHELIN, M., EL ALBANI, A.,
549 GAUTHERON, C., IZART, A., JANOTS, D., MICHELS, R., PAGEL, M., POZZI, J.-P., BOIRON, M.-C., AND LANDREIN, P. 2014.
550 Reconstruction of low temperature (<100 °C) burial in sedimentary basins. A comparison of
551 geothermometer in the intracontinental Paris Basin. *Marine and Petroleum Geology* 53, 71–87.
- 552 BOISSAVY, C., AND GRIÈRE, O. 2014. New Geothermal Targets in the Paris Basin (France). *GRC Transactions* 38,
553 577-582.
- 554 BONIFACIE, M., CALMELS, D., EILER, J.M., HORITA, J., CHADUTEAU, C., VASCONCELOS, C., AGRINIER, P., KATZ, A., PASSEY,
555 B.H., FERRY, J.M., AND BOURRAND, J.-J. 2017. Calibration of the dolomite clumped isotope thermometer
556 from 25 to 350 °C, and implications for a universal calibration for all (Ca, Mg, Fe)CO₃ carbonates.
557 *Geochimica et Cosmochimica Acta* 200, 255–279.
- 558 BONTE, D., GUILLOU-FROTTIER, L., GARIBALDI, C., BOURGINE, B., LOPEZ, S., BOUCHOT, V., AND LUCAZEAU, F. 2010.
559 Subsurface temperature maps in French sedimentary basins: new data compilation and interpolation.
560 *Bulletin de la Société Géologique de France* 181, 4, 377–390.
- 561 BOURGEOIS, O., FORD, M., DIRAISON, M., DE VESLUD, C. L. C., GERBAULT, M., PIK, R., ... & BONNET, S. 2007.
562 Separation of rifting and lithospheric folding signatures in the NW-Alpine foreland. *International Journal*
563 *of Earth Sciences*, 96 (2007), 1003–1031.
- 564 BRUNET, M. F., AND LE PICHON, X. 1982. Subsidence of the Paris Basin. *Journal of Geophysical research*, 87,
565 8547–8560.
- 566 CARR, A.D. 2000. Suppression and retardation of vitrinite reflectance, Part 1. Formation and significance for
567 hydrocarbon generation. *Journal of Petroleum Geology*, 23, 313–343.

568 CONTOUX, C., VIOLETTE, S., VIVONA, R., GOBLET, P., AND PATRIARCHE, D. 2013. How basin model results enable the
569 study of multi-layer aquifer response to pumping. The Paris Basin, France. *Hydrogeol J* 21, 3, 545–557.

570 CURNELLE, R., AND DUBOIS, P. 1986. *Évolution mésozoïque des grands bassins sédimentaires Français. bassins*
571 *de Paris, d'Aquitaine et du Sud-Est. Bulletin de la Société géologique de France*, 2(4), 529-546.

572 DEBEGLIA, N. 1977. *Rapport the synthèse géophysique a la connaissance du socle du bassin de Paris. Bureau*
573 *de recherches géologiques et minière. Service géologique national. Report BRGM/77-SGN535-GPH..*

574 DELMAS, J., P. HOUEL, AND R. VIALLY. 2002. Paris Basin. *Petroleum Potential (IFPEN Regional Report) - Rapport*
575 *Régional D'évaluation Pétrolière).Institut Français du Pétrole report n°61121.*

576 DEMARS, C. & PAGEL, M. 1994. Paléotempératures et paléosalinités dans les grès du Keuper du Bassin de
577 Paris: inclusions fluides dans les minéraux authigènes. *Compt. Rendus Acad. Sci. Paris*, 2 (1994), 427–434.

578 DEMBICKI, J.H. 2016. Basin Modeling. In *Practical petroleum geochemistry for exploration and production*, H.
579 DEMBICKI, Ed. Elsevier, Waltham MA, 273–308.

580 DEMING, D. 1989. Application of bottom-hole temperature corrections in geothermal studies. *Geothermics*
581 18, 5-6, 775–786.

582 DEMONGODIN, L., PINOTEAU, B., VASSEUR G., AND GABLE, R. 1991. Thermal conductivity and well logs: a case
583 study in the Paris basin. *Geophysical Journal International* 105, 675–691.

584 DENNIS, K.J., AND SCHRAG, D.P. 2010. Clumped isotope thermometry of carbonatites as an indicator of
585 diagenetic alteration. *Geochimica et Cosmochimica Acta* 74, 14, 4110–4122.

586 DENTZER, J., LOPEZ, S., VIOLETTE, S., AND BRUEL, D. 2016. Quantification of the impact of paleoclimates on the
587 deep heat flux of the Paris Basin. *Geothermics* 61, 35–45.

588 DUWIKUET, H., ARBARET, L., GUILLOU-FROTTIER, L., HEAP, M. J., AND BELLANGER, M. 2019. On the geothermal
589 potential of crustal fault zones: a case study from the Pontgibaud area (French Massif Central, France).
590 *Geothermal Energy*, 7(1), 33.

591 GABLE, R. 1978. *Acquisition et rassemblement de données géothermiques disponibles en France. Contrat*
592 *170-76 egf - projet g/a 5. Bureau de Recherches Géologiques et Minières . Report BRGM/78-SGN-284-*
593 *GTH, 60 p. 1 pht., 10 maps.*

594 GABLE, R. 1979. *Température, gradient et flux de chaleur terrestre, mesures, interprétation. Bureau de*
595 *Recherches Géologiques et Minières. Report 104, BRGM.*

596 GABLE, R. 1988. *Thermicité du bassin de Paris. Bureau de Recherches Géologiques et Minières . Bureau de*
597 *Recherches Géologiques et Minières. Report BRGM/89-DT-004-GPH.*

598 GABLE, R. 1989. *Thermicité du bassin de Paris. Bureau de Recherches Géologiques et Minières. RAPPORT*
599 *TECHNIQUE : CAMPAGNES DE MESURES/1988 . BRGM/89-DT-004-GPH, 16 p. 3 cartes.*

600 GABLE, R., FOUCHER, J.C., MENJOZ, A., PHILIP, J.M., & ROIGNOT, G. 1982. *Mesures, analyse et interprétation de*
601 *profils thermiques. Application à la détermination des températures in-situ. Bureau de Recherches*
602 *Géologiques et Minières . BRGM/82-SGN-413-GTH, 55 p. 10 pht., 8 cartes.*

603 GAULIER, J.-M., AND BURRUS, J. 1994. Modeling Present and Past Thermal Regimes in the Paris Basin.
604 *Petroleum Implications. Hydrocarbon and Petroleum Geology of France. Springer, Berlin, Heidelberg,, 61–*
605 *73.*

606 GHOSH, P., ADKINS, J., AFFEK, H., BALTA, B., GUO, W., SCHAUBLE, E.A., SCHRAG, D., AND EILER, J.M. 2006. 13C–18O
607 bonds in carbonate minerals. A new kind of paleothermometer. *Geochimica et Cosmochimica Acta* 70, 6,
608 1439–1456.

609 GONÇALVES, J. 2002. *Modélisation 3D de l'évolution géologique du bassin de Paris: implications*
610 *diagénétiques et hydrodynamiques [3D model of the Paris Basin geological evolution : diagenetic and*
611 *hydrodynamic implications]. PhD Thesis, University Pierre and Marie Curie, Paris, France, 351 pp.*

612 GONÇALVES, J., VIOLETTE, S., ROBIN, C., PAGEL, M., GUILLOCHEAU, F., DE MARSILY, G., ... & LEDOUX, E. (2003). 3-D
613 modelling of salt and heat transport during the 248 my evolution of the Paris basin: diagenetic
614 implications. *Bulletin de la Société géologique de France*, 174(5), 429-439.

615 GONÇALVES, J., PAGEL, M., VIOLETTE, S., GUILLOCHEAU, F., AND ROBIN, C. 2010. Fluid inclusions as constraints in a
616 three-dimensional hydro-thermo-mechanical model of the Paris basin, France. *Basin Research* 22, 5,
617 699–716.

618 GONÇALVÈS, J., VIOLETTE, S., GUILLOCHEAU, F., ROBIN, C., PAGEL, M., BRUEL, D., MARSILY, G. de, and LEDOUX, E. 2004.
619 Contribution of a three-dimensional regional scale basin model to the study of the past fluid flow
620 evolution and the present hydrology of the Paris basin, France. *Basin Research* 16, 4, 569–586.

621 GUILHAUMOU, N. 1993. Paleotemperatures inferred from fluid inclusions in diagenetic cements. Implications
622 for the thermal history of the Paris basin. *Eur. J. Mineral* 5, 1217–1226.

623 GUILHAUMOU, N., & GAULIER, J. M. 1991. *Détermination de paléotempératures dans les roches-mères du*
624 *bassin de Paris: étude d'inclusions fluides et implications pour l'histoire thermique du bassin*. Comptes
625 rendus de l'Académie des sciences. Série 2, Mécanique, Physique, Chimie, Sciences de l'univers, Sciences
626 de la Terre, 313(7), 773-780.

627 GUILLOCHEAU, F. 1991. Mise en évidence de grands cycles transgression-régression d'origine tectonique dans
628 les sédiments mésozoïques du Bassin de Paris. *Comptes rendus de l'Académie des sciences. Série 2,*
629 *Mécanique, Physique, Chimie, Sciences de l'univers, Sciences de la Terre* 312, 13, 1587–1593.

630 GUILLOCHEAU, F., ROBIN, C., ALLEMAND, P., BOURQUIN, S., BRAULT, N., DROMART, G., FRIEDENBERG, R., GARCIA, J.-P.,
631 GAULIER, J.-M., GAUMET, F., GROSDOY, B., HANOT, F., LE STRAT, P., METTRAUX, M., NALPAS, T., PRIJAC, C., RIGOLTET,
632 C., SERRANO, O., AND GRANDJEAN, G. 2015. Meso-Cenozoic geodynamic evolution of the Paris Basin. 3D
633 stratigraphic constraints. *Geodinamica Acta* 13, 4, 189–245.

634 HABICHT, J.K.A. 1979. Paleoclimate, paleomagnetism and continental drift. *American Association of*
635 *Petroleum Geologists. Studies in Geology No. 9. x + 29 pp., 11 foldout plates.*JONES, R. W., EDISON, A. 1979.
636 Microscopic observations of kerogene related to geochemical parameters with emphasis on thermal
637 maturation. *Society Economic Paleontologists and Mineralogists*, 1–12.

638 JOST, A., VIOLETTE, S., GONÇALVÈS, J., LEDOUX, E., GUYOMARD, Y., GUILLOCHEAU, F., KAGEYAMA, M., RAMSTEIN, G., AND
639 SUC, J.-P. 2007. Long-term hydrodynamic response induced by past climatic and geomorphologic forcing.
640 The case of the Paris basin, France. *Physics and Chemistry of the Earth, Parts A/B/C* 32, 1-7, 368–378.

641 KELE, S., BREITENBACH, S.F.M., CAPEZZUOLI, E., MECKLER, A.N., ZIEGLER, M., MILLAN, I.M., KLUGE, T., DEÁK, J.,
642 HANSELMANN, K., JOHN, C.M., YAN, H., LIU, Z., AND BERNASCONI, S.M. 2015. Temperature dependence of
643 oxygen- and clumped isotope fractionation in carbonates. A study of travertines and tufas in the 6–95°C
644 temperature range. *Geochimica et Cosmochimica Acta* 168, 172–192.

645 LAVASTRE, V., LE SALLE, C.G., MICHELOT, J.-L., GIANNESINI, S., BENEDETTI, L., LANCELLOT, J., LAVIELLE, B., MASSAULT, M.,
646 THOMAS, B., GILABERT, E., BOURLÈS, D., CLAUER, N., AND AGRINIER, P. 2010. Establishing constraints on
647 groundwater ages with ³⁶Cl, ¹⁴C, ³H, and noble gases. A case study in the eastern Paris basin, France.
648 *Applied Geochemistry* 25, 1, 123–142.

649 LE SOLLEUZ, A., DOIN, M.-P., ROBIN, C., AND GUILLOCHEAU, F. 2004. From a mountain belt collapse to a
650 sedimentary basin development. 2-D thermal model based on inversion of stratigraphic data in the Paris
651 Basin. *Tectonophysics* 386, 1-2, 1–27.

652 LOPEZ, S., HAMM, V., LE BRUN, M., SCHAPER, L., BOISSIER, F., COTICHE, C., AND GIUGLARIS, E. 2010. 40 years of
653 Dogger aquifer management in Ile-de-France, Paris Basin, France. *Geothermics* 39, 339–356.

654 LOUP, B., AND WILDI, W. 1994. Subsidence analysis in the Paris Basin: a key to Northwest European
655 intracontinental basins? *Basin Research* 6, 2-3, 159–177.
656 <http://www.earthdoc.org/publication/download/?publication=62612>.

657 LUCAZEAU, F., AND VASSEUR, G. 1989. Heat flow density data from France and surrounding margins.
658 *Tectonophysics* 164, 2-4, 251–258.

659 MANGENOT, X., BONIFACIE, M., GASPARRINI, M., GÖTZ, A., CHADUTEAU, C., ADER, M., AND ROUCHON, V. 2017.
660 Coupling $\Delta 47$ and fluid inclusion thermometry on carbonate cements to precisely reconstruct the
661 temperature, salinity and $\delta 18 O$ of paleo-groundwater in sedimentary basins. *Chemical Geology* 472,
662 44–57.

663 MANGENOT, X., GASPARRINI, M., ROUCHON, V., BONIFACIE, M., AND FRANK, T. 2018. Basin-scale thermal and fluid
664 flow histories revealed by carbonate clumped isotopes ($\Delta 47$) - Middle Jurassic carbonates of the Paris
665 Basin depocentre. *Sedimentology* 65, 1, 123–150.

666 MARTELET, G., PERRIN, J., TRUFFERT, C., AND DEPARIS, J. 2013. Fast mapping of magnetic basement depth,
667 structure and nature using aeromagnetic and gravity data. Combined methods and their application in
668 the Paris Basin. *Geophysical Prospecting* 61, 4, 857–873.

669 MARTY, B., TORGERSEN, T., AND MEYNIER, V. 1993. Helium isotope fluxes and groundwater ages in the Dogger
670 Aquifer, Paris Basin. *Water Resources Research* 29, 4, 1025–1035.

671 MCTAVISH, R.A. 1978. Pressure retardation of vitrinite diagenesis, offshore north-west Europe. *Nature*, 271,
672 648–650.

673 MEGNIEN, C. 1980. Tectogenese du Bassin de Paris; etapes de l'evolution du bassin. *Bulletin de la Société*
674 *Géologique de France S7-XXII*, 4, 669–680.

675 MONNET, M. 2006. *Inventaire des températures et des salinités des aquifères du dogger calcaire et du trias*
676 *gréseux dans le secteur d'étude de picoref (bassin de Paris, champagne méridionale)*. IFPEN Rapport
677 Interne n°59466.

678 OBERLIN, A., BOULMIER, J.L., and VILLEY, M., 1980. Electron microscopic study of kerogen microtexture.
679 Selected criteria for determining the evolution path and evolution stage of kerogen. In: (Durand B., ed.),
680 Kerogen, Editions Technip, Paris, p. 191-242.

681 PANZA, G.F., ST. MUELLER, AND CALCAGNILE, G. 1980. The gross features of the lithosphere-asthenosphere
682 system in Europe from seismic surface waves and body waves. *PAGEOPH* 118, 2, 1209–1213.

683 PERRODON, A., & ZABEK, J. 1990. Paris Basin: Chapter 32: Part II. Selected Analog Interior Cratonic Basins.
684 Analog Basins, *AAPG Mem.* 51. 633–679.

685 POLLACK, H.N. 1982. The Heat Flow from the Continents. *Annu. Rev. Earth Planet. Sci.* 10, 1, 459–481.

686 PRIJAC, C., DOIN, M.P., GAULIER, J.M., AND GUILLOCHEAU, F. 2000. Subsidence of the Paris Basin and its bearing
687 on the late Variscan lithosphere evolution: a comparison between Plate and Chablis models.
688 *Tectonophysics*, 323, 1–38.

689 PURSER, B.H. 1975. *Sédimentation et diagenèse précoce des séries carbonatées du Jurassique moyen de*
690 *Bourgogne*. PhD thesis University Paris sud, 383 pp.

691 RÉVEILLÈRE, A., HAMM, V., LESUEUR, H., CORDIER, E., AND GOBLET, P. 2013. Geothermal contribution to the energy
692 mix of a heating network when using Aquifer Thermal Energy Storage: Modeling and application to the
693 Paris basin. *Geothermics* 47, 69–79.

694 RUDNICK, R.L. AND FOUNTAIN, D., M. 1995a. Nature and Composition of the Continental Crust; A Lower Crustal
695 Perspective. *Reviews of geophysics*, 33(3), 267-309.

696 ROEDDER, E. 1984. Fluid Inclusion. Reviews in Mineralogy. *Mineral. Soc. of America*, 12, 644 pp.

697 SCHNEIDER, F., POTDEVIN, J. L., WOLF, S., & FAILLE, I. (1996). MECHANICAL AND CHEMICAL COMPACTION MODEL FOR
698 SEDIMENTARY BASIN SIMULATORS. *TECTONOPHYSICS*, 263(1-4), 307-317.

699 SOUCHE, A., SCHMID, D.W., AND RÜPKE, L. 2017. Interrelation between surface and basement heat flow in
700 sedimentary basins. *Bulletin* 101, 10, 1697–1713.

701 SWEENEY, J. J., & BURNHAM, A. K. 1990. Evaluation of a simple model of vitrinite reflectance based on
702 chemical kinetics. *AAPG bulletin*, 74(10), 1559-1570.

- 703 TELES, V., FORNEL, A., HOUEL, P., DELMAS, J., MENGUS, J.M., MICHEL, A., AND MAURAND, N. 2014. Coupling Basin
704 and Reservoir Simulators for an Improved CO2 Injection Flow Model. *Energy Procedia* 63, 3665–3675.
- 705 TESAURO, M., KABAN, M.K., AND CLOETINGH, S.A.P.L. 2009. A new thermal and rheological model of the
706 European lithosphere. *Tectonophysics* 476, 3-4, 478–495.
- 707 THEISSEN, S., AND RÜPKE, L.H. 2009. Feedbacks of sedimentation on crustal heat flow. New insights from the
708 Vøring Basin, Norwegian Sea. *Basin Research* 167, 327.
- 709 THOMAS, J., FROST, R.R., AND HARVEY, R.D. 1973. Thermal conductivity of carbonate rocks. *Engineering Geology*
710 7, 1, 3–12.
- 711 TISSOT, B.P., PELET, R., UNGERER, PH. 1987. Thermal History of Sedimentary Basins, Maturation Indices, and
712 Kinetics of Oil and Gas Generation. *AAPG Bulletin* 71, 12, 1445–1466.
713 <http://archives.datapages.com/data/bulletns/1986-87/images/pg/00710012/1400/14450.pdf>.
- 714 URIARTE, J.A. 1997. *Maturité thermique des sédiments de la bordure sud-est du Bassin de Paris*, University of
715 Geneva. PhD thesis. 146 pp.
- 716 VAN HINSBERGEN, D.J.J., LENNART V. DE GROOT, SEBASTIAAN J. VAN SCHAİK, WIM SPAKMAN, PETER K. BIJL, APPY SLUIJS,
717 COR G. LANGEREIS, AND HENK BRINKHUIS. 2015. *A Paleolatitude Calculator for Paleoclimate Studies*. PloS one,
718 2015, vol. 10, no 6
- 719 WEBER, C. 1973. *Les granitoïdes du Sud du Bassin de Paris; données hypogéologiques obtenues par la*
720 *géophysique*. Bulletin de la Société Géologique de France, 1973, vol. 7, no 3-4, p. 252-259.
- 721 WELTE, D.H., HORSFIELD, B., AND BAKER, D.R., Eds. 1997. *Petroleum and Basin Evolution. Insights from*
722 *Petroleum Geochemistry, Geology and Basin Modeling*. Springer Berlin Heidelberg, Berlin, Heidelberg.
723 535 pp.
- 724 WENDEBOURG, J., AND LAMIRAUX, C. 2002. Estimating the Ultimate Recoverable Reserves of the Paris Basin,
725 France. *Oil & Gas Science and Technology* 57, 6, 621–629.
- 726 ZIEGLER, P.A. 1980. *North Western Europe: Subsidence patterns of Post-Variscan basins*. In Cogné, J.; Slansky,
727 M. (eds.). *Géologie de l'Europe du Précambrien aux bassins sédimentaire post-hercyniens*. Mém. BRGM.
728 108. pp. 249–280.
- 729 ZIEGLER, P.A. 1988. *Evolution of The Artic-North Atlantic and the Western Tethys - American Association of*
730 *Petroleum Geologists Memoir*. 43.

731

732 FIGURE

733

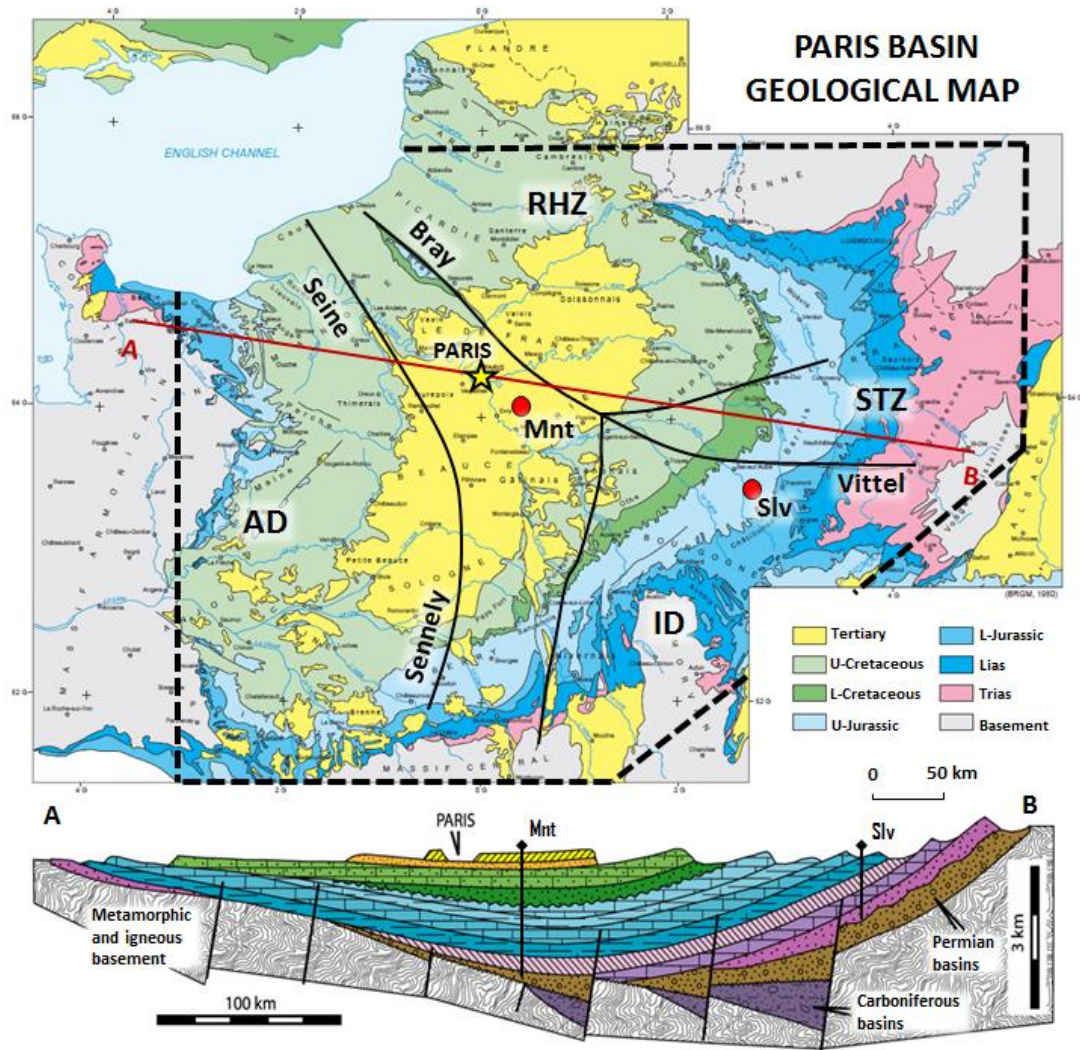
734

735

736

737

738



739

740 *Figure 1. Geological map and cross-section of the Paris Basin modified after Delmas et al., (2002)*
 741 *and Beccaletto et al. [2011]. The basement domains (AD – Armorican Domain, ID – Internal*
 742 *Domain, STZ – Saxo-Thuringian Zone, RHZ – Rheno-Hercynian Zone) are structured by the main*
 743 *faults (the N-E Bray-Vittel fault and the NW-S Seine-Sennely fault). Note that these faults are not*
 744 *affecting the present-day sedimentary cover. The dashed black polygon represents the modeled*
 745 *domain. The cross section shows the projected location of Montlevée well (Mnt) and Silvarouvres*
 746 *well (Slv).*

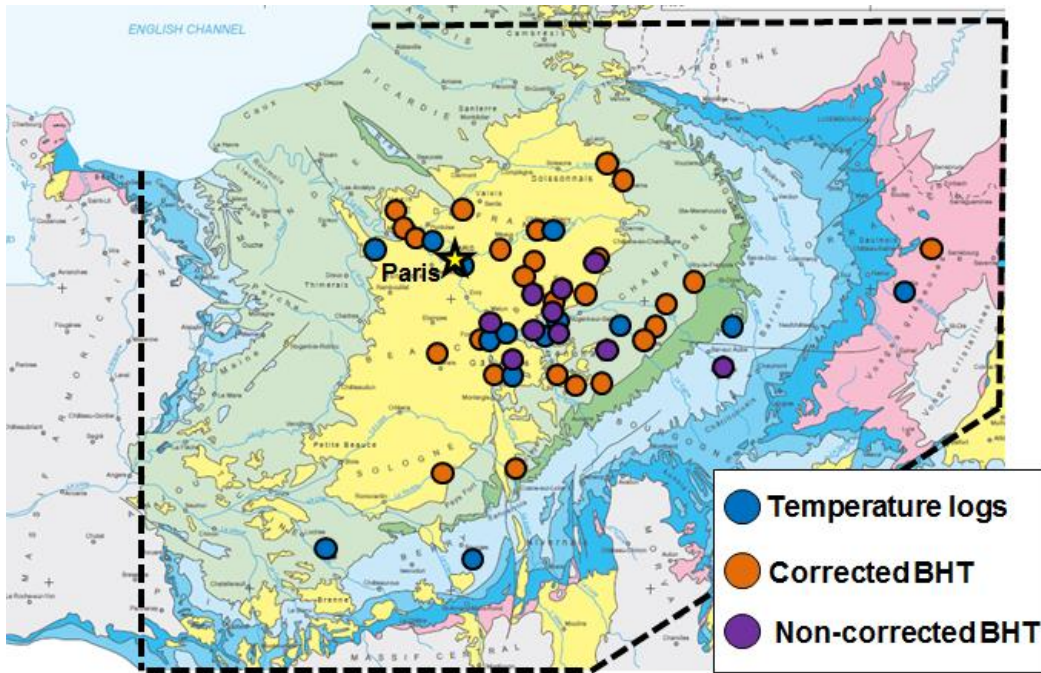
747

(2 columns)

748

749

750



751

752 *Figure 2. Map of the Paris Basin and regional distribution of the main wells used for the present-*
 753 *day thermal calibration. The domain of the model is delimited by the black polygon.*

754

(1 column)

755

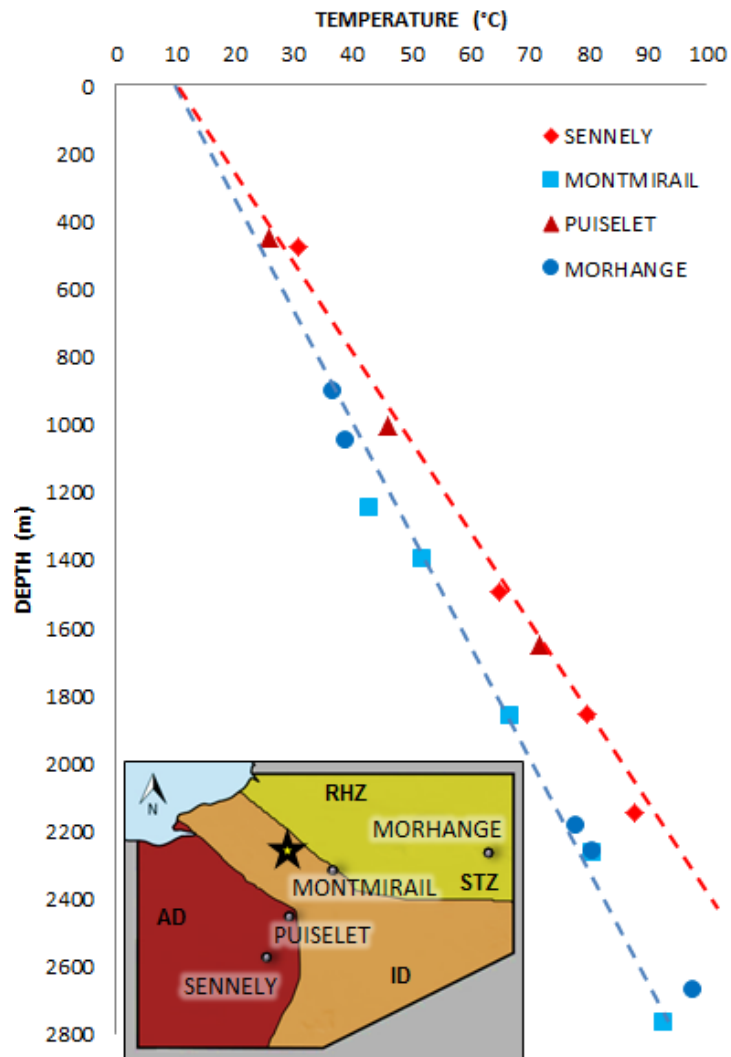
756

757

758

759

760



761

762 *Figure 3. Depth vs temperature for various wells overlying different basement domains (detailed*
 763 *information on these domains is given in Table III). The yellow star indicates the location of the city*
 764 *of Paris. The temperatures in Sennely and Puisselet (red symbols) are higher than those in*
 765 *Montmirail and Morhange (blue symbols). The blue dashed line indicates the average geothermal*
 766 *gradient of the colder area of 30°C/km. The red dashed line indicates the average geothermal*
 767 *gradient measured in the warmer area, corresponding to 40°C/km.*

768

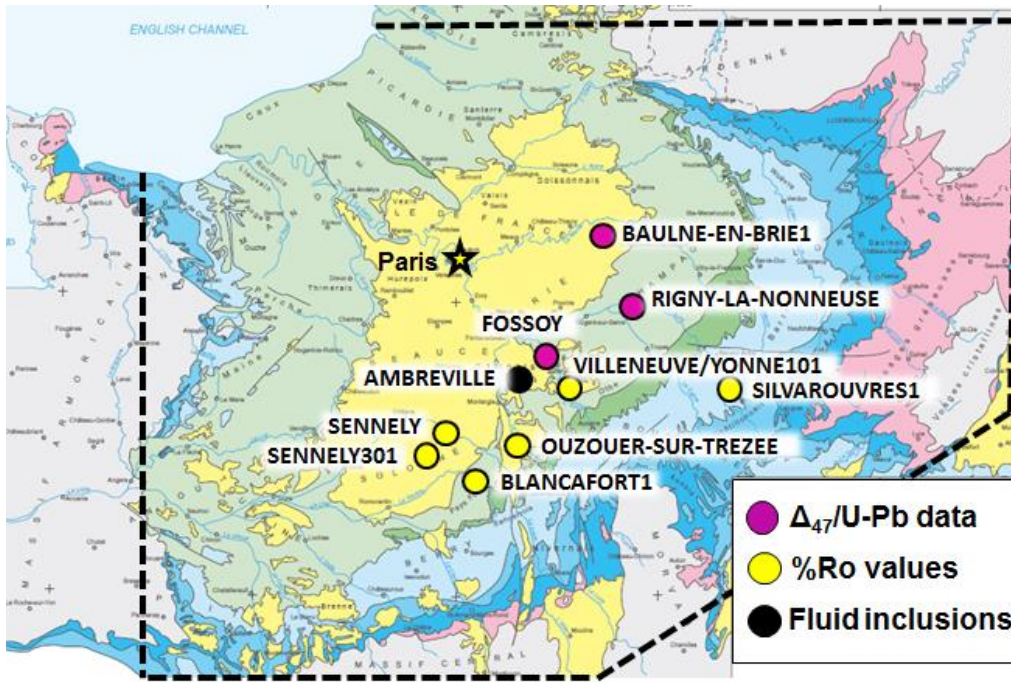
769

770

771

772

773



774

775 *Figure 4. Map of the Paris Basin and locations of wells used for the paleo-thermal regime*
 776 *calibration. The yellow star represents Paris. The domain of the model is delimited by the black*
 777 *polygon.*

778

(1 column)

779

780

781

782

783

784

785

786

787

788

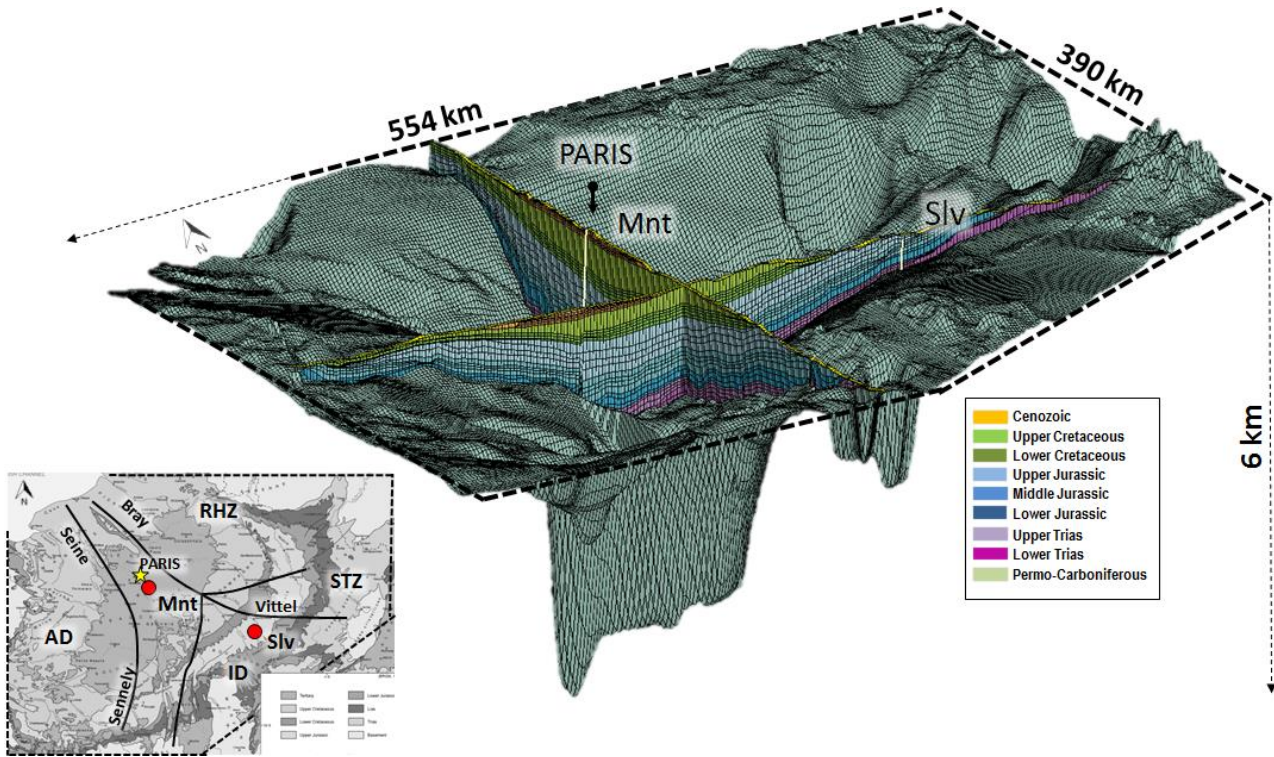
789

790

791

792

793
794
795



796

797 *Figure 5. Structural geometry of the 3D model of the Paris Basin as constructed in TemisFlow. The*
798 *model covers a surface of about 200.000 km². The insert map is from Figure 1 and shows*
799 *Montlevée (Mnt) and Silvarouvres (Slv) well locations. The shape of the basement shows the deep*
800 *Permo-Carboniferous troughs underlying the Paris basin. The outcropping sedimentary cover is*
801 *asymmetric as the result of the Upper Cretaceous erosion event which mainly affected the eastern*
802 *flank of the basin.*

803

(2 column)

804

805

806

807

808

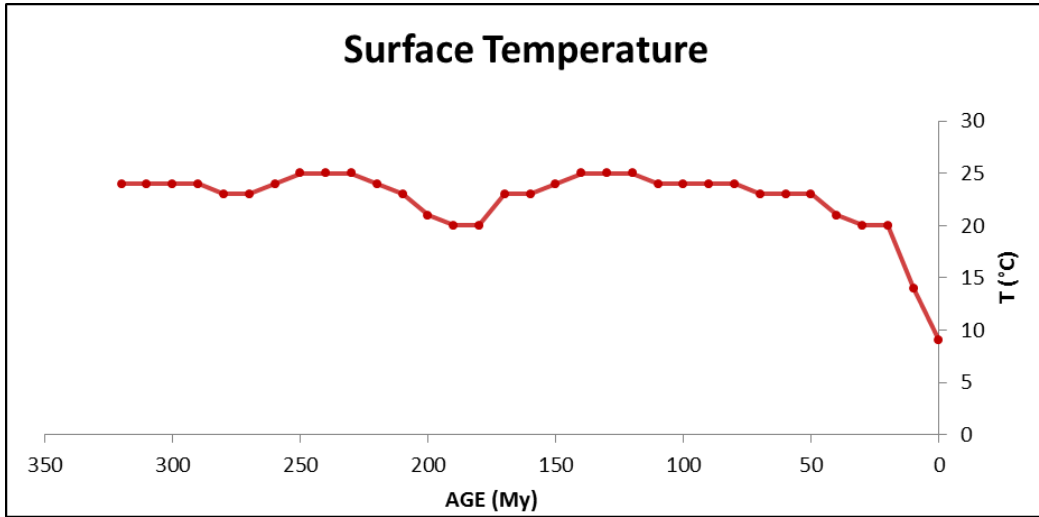
809

810

811

812

813
814
815



816

817 *Figure 6. Surface temperatures through time as used in the TemisFlow model. The temperature at*
818 *each time step is determined from the Paleo-latitude Calculator for Paleoclimate Studies [van*
819 *Hinsbergen et al. 2015]. The basin is characterized by tropical temperatures until the last 20 My.*

820

(1 column)

821

822

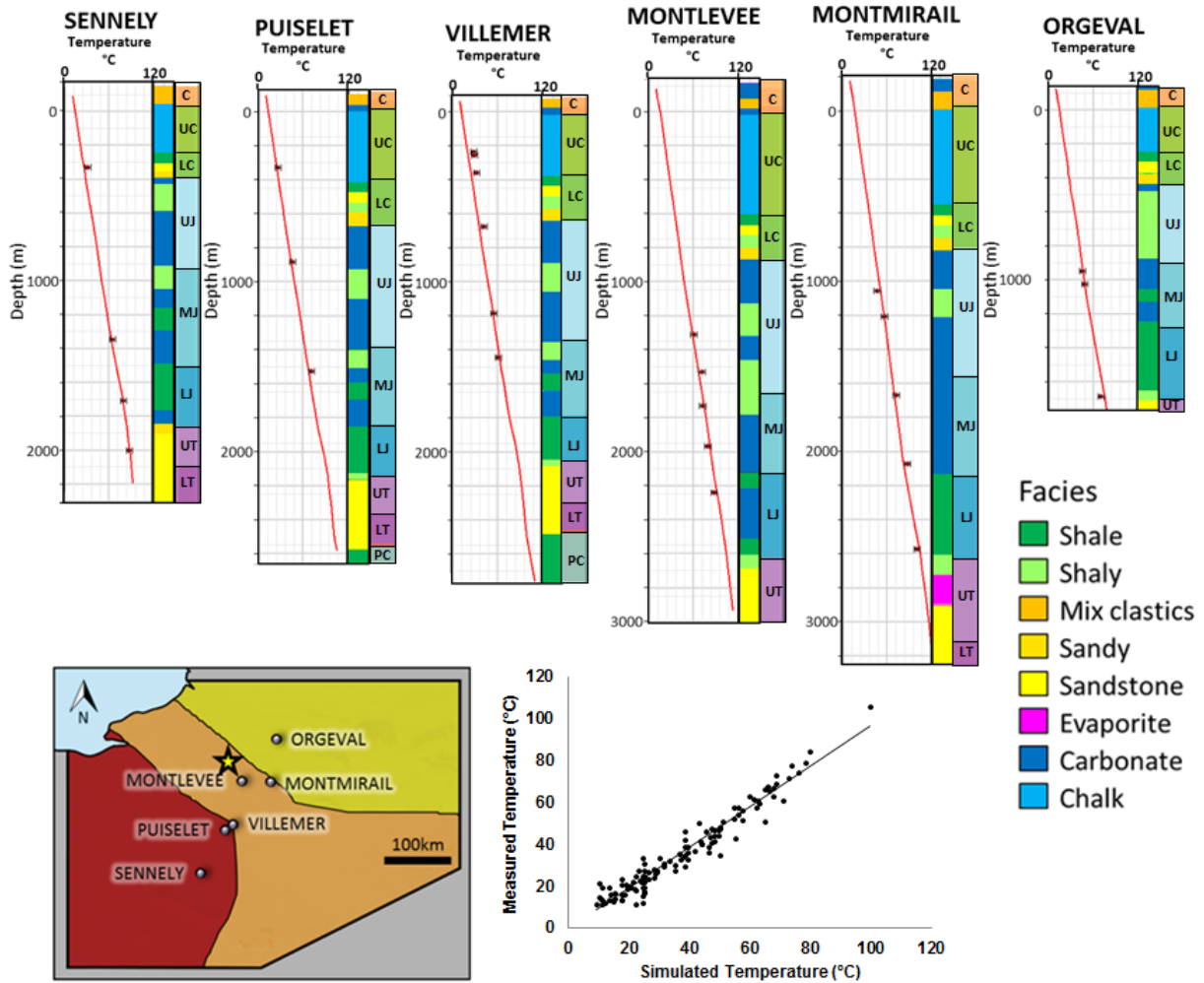
823

824

825

826

827



828

829 *Figure 7. Temperature calibration results for 6 wells with corrected BHT values. The first column*
 830 *represents the lithology and the second column the age (PC=Permo-Carboniferous; LT=Lower*
 831 *Triassic; UT=Upper Triassic; LJ=Lower Jurassic; MJ=Middle Jurassic; UJ=Upper Jurassic; LC=Lower*
 832 *Cretaceous; UP=Upper Cretaceous; C=Cenozoic). The modeled temperature (red line) remains*
 833 *within the uncertainty range both in the shallow and the deep parts of the wells. Cross-plot shows*
 834 *measured vs simulated temperature ($R^2 = 0.9431$) for the 14 wells with temperature logs [Gable et*
 835 *al. 1982; 1988, 1989] whose well locations are shown in Figure 2.*

836

(2 columns)

837

838

839

840

841

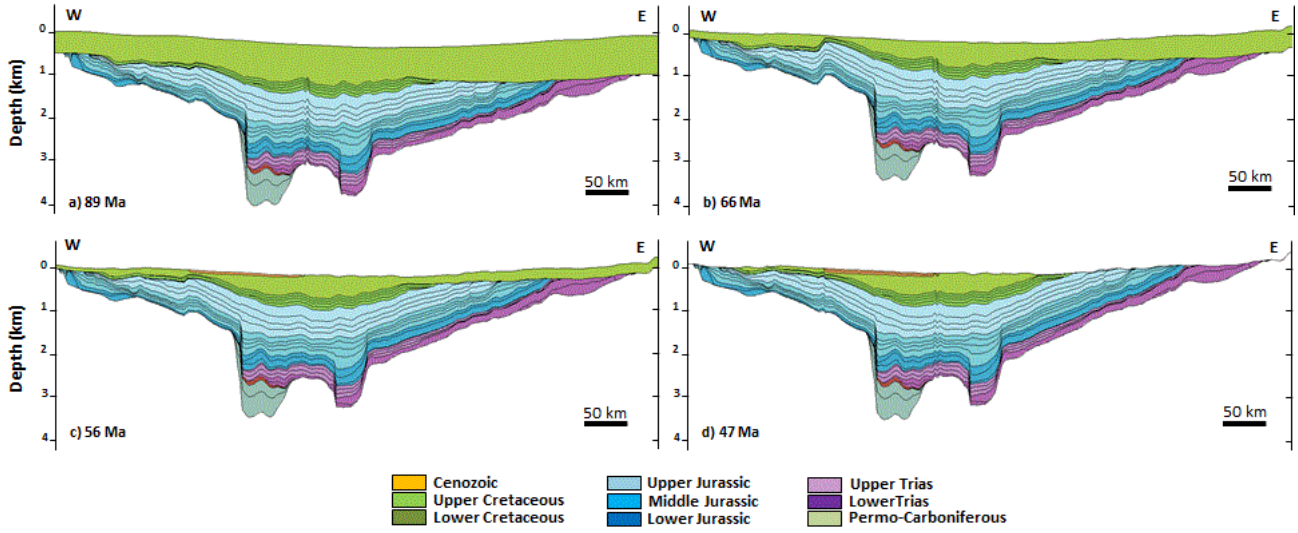
842

843

844

845

846



847

848 *Figure 8. Evolution of the burial during the Upper Cretaceous/Tertiary. The location of the 2D*
849 *section A-A' is shown in figure 9.*

850

(2 column)

851

852

853

854

855

856

857

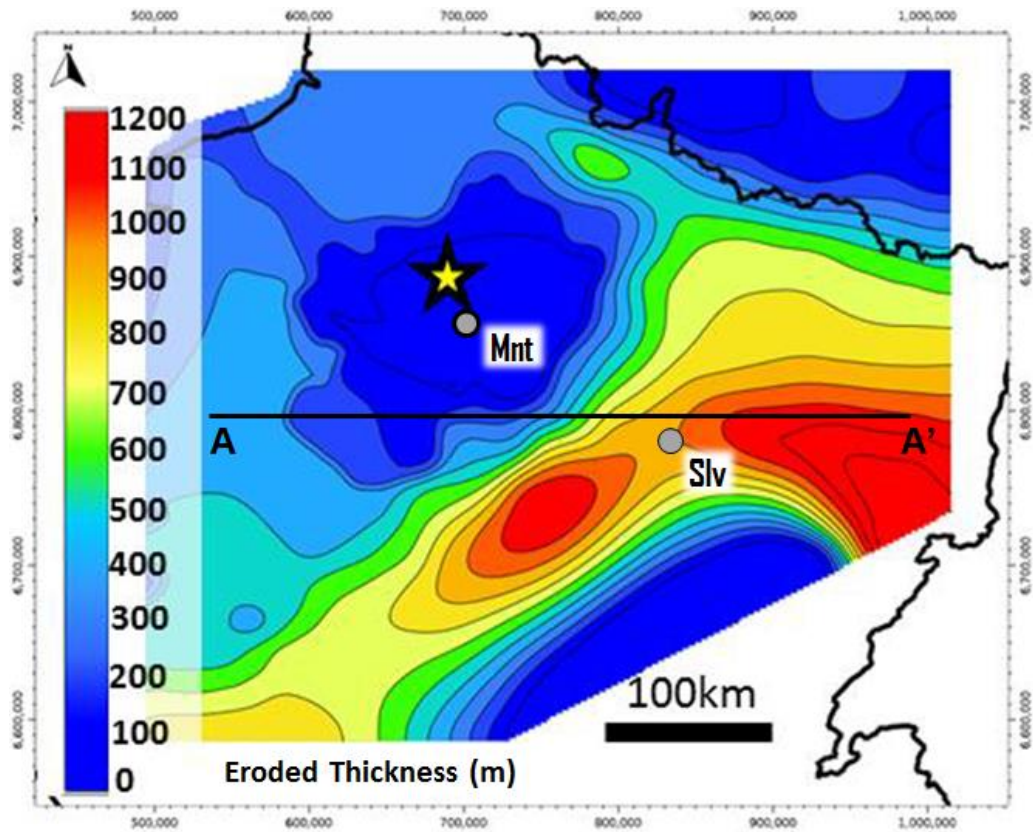
858

859

860

861

862



863

864 *Figure 9. Total eroded thickness map during the Upper Cretaceous/Tertiary. The yellow star*
 865 *represents the location of Paris. The erosion started during the Upper Cretaceous (66 Ma) and*
 866 *continued until the Ypresian (47.8 Ma). The event affected more the border of the basin where the*
 867 *total eroded thickness reached > 1000 m. Mnt=Montelée well; Slv=Silvarouvres well.*

868

(1 column)

869

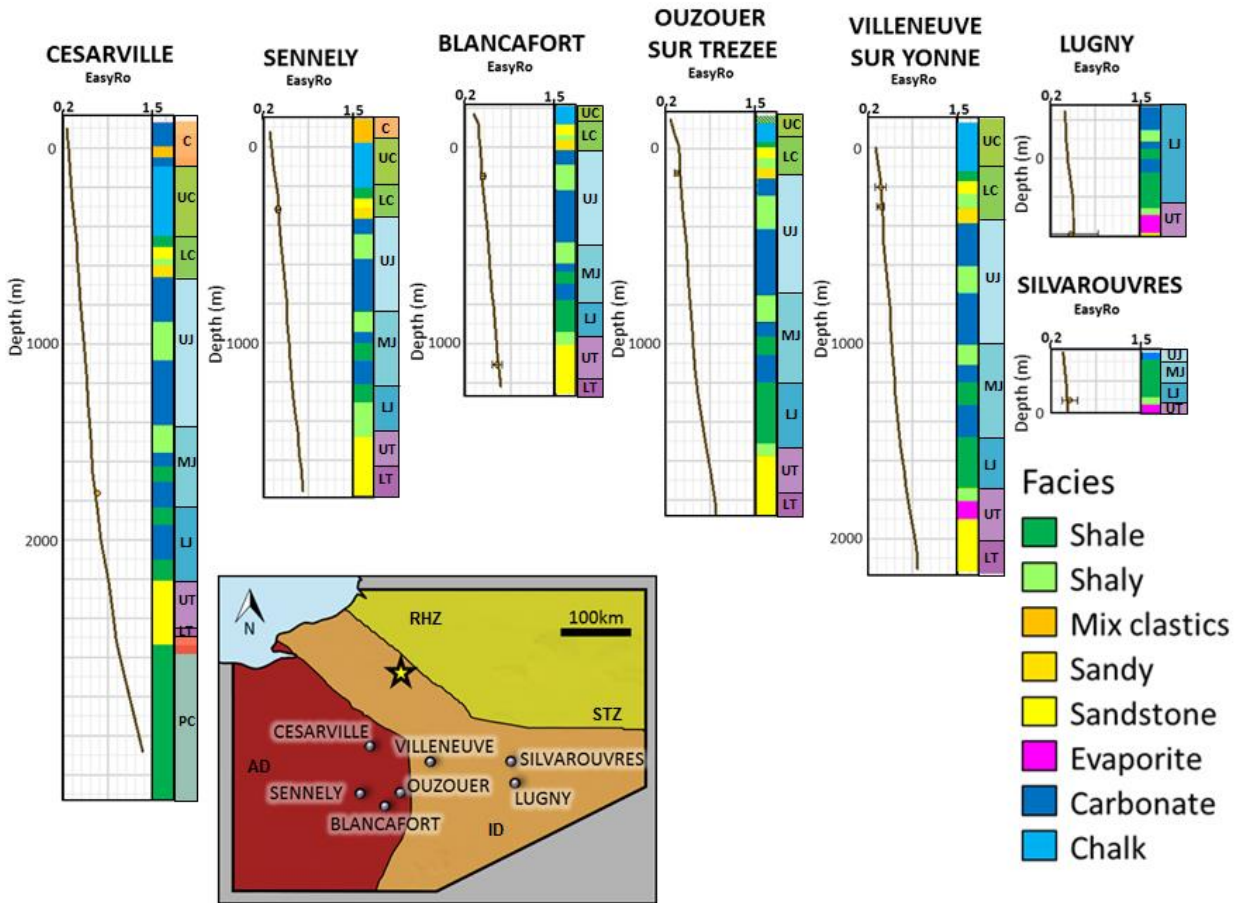
870

871

872

873

874



875

876 *Figure 10. Paleo-thermal calibration results of vitrinite reflectance data taken from Uriarte [1997].*
 877 *The first column represents lithology and the second column age (PC=Permo-Carboniferous;*
 878 *LT=Lower Triassic; UT=Upper Triassic; LJ=Lower Jurassic; MJ=Middle Jurassic; UJ=Upper Jurassic;*
 879 *LC=Lower Cretaceous; UP=Upper Cretaceous; C=Cenozoic).The modeled maturities (brown curve)*
 880 *show a good fit for all the wells, as they remain within the standard deviation values for each*
 881 *vitrinite reflectance data point.*

882

(2 columns)

883

884

885

886

887

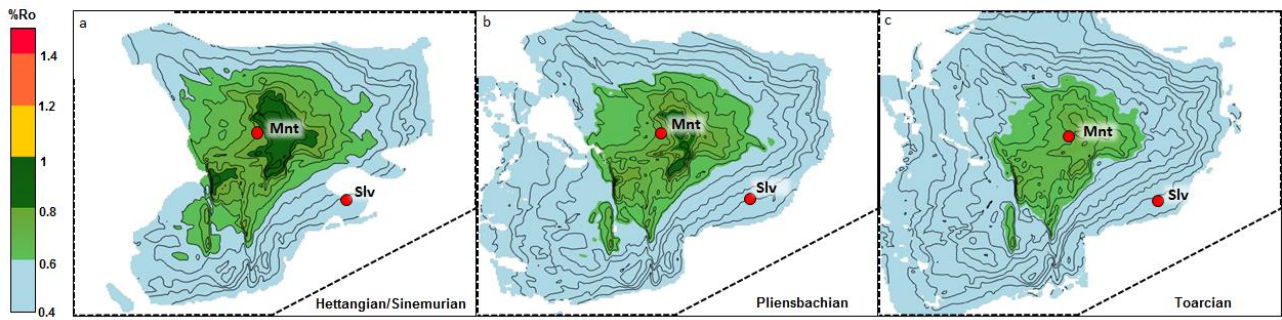
888

889

890

891

892



893

894 *Figure 11. Present-day maturity map for the Liassic source rock. a) Hettangian/Sinemurian; b)*
895 *Pliensbachian; c) Toarcian (Schistes Carton). The wells are also shown along the cross-section in*
896 *Figure 1 and Figure 9 (Mnt=Montelée well; Slv=Silvarouvres well).*

897

(2 columns)

898

899

900

901

902

903

904

905

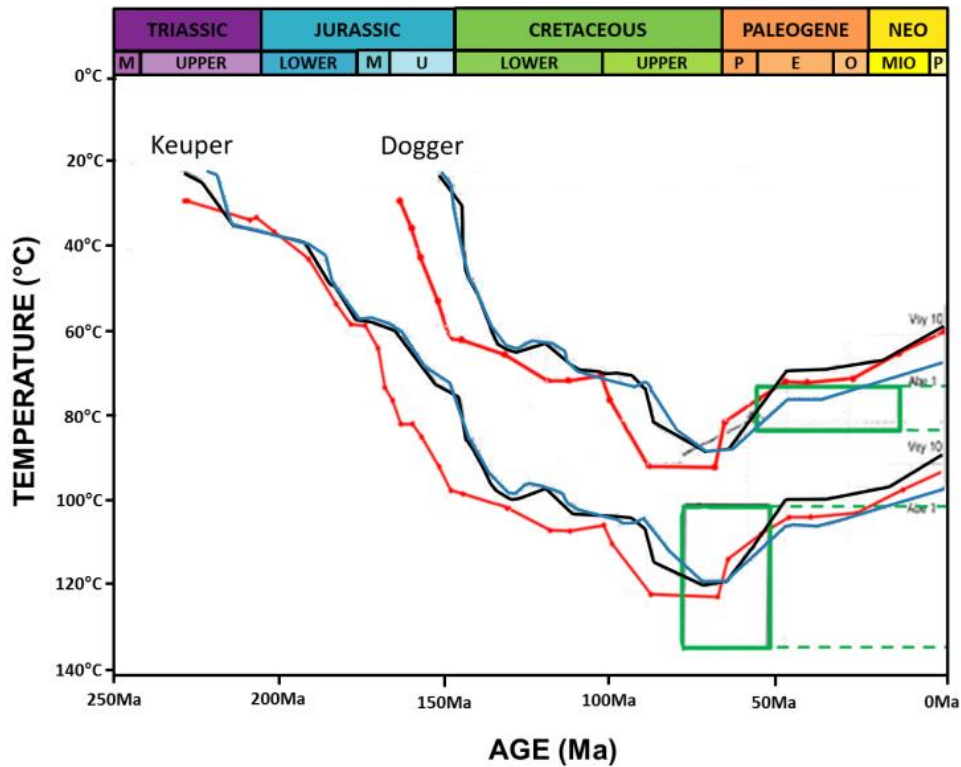
906

907

908

909

910



911

912 *Figure 12. Modeled temperature histories compared with temperatures estimated from fluid*
 913 *inclusions (Guilhaumou 1993) (green rectangle) and temperature evolution over time for*
 914 *Villeneuve sur Yonne (black line) and Ambreville well (blue line) (Uriarte 1997). The modeled*
 915 *temperature (red line) is extracted from Ambreville well for the Triassic and the Dogger that*
 916 *reached a maximum temperature of 125/130°C and 90/95°C respectively during the Upper-*
 917 *Cretaceous time.*

918

(1 column)

919

920

921

922

923

924

925

926

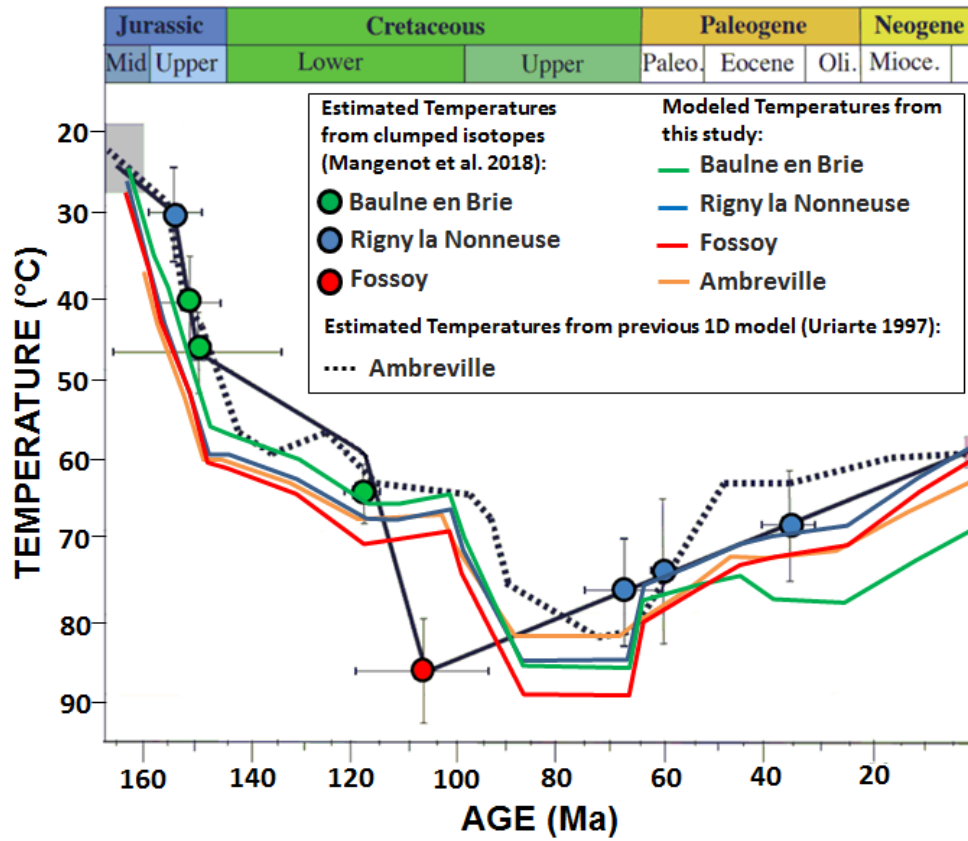
927

928

929

930

931



932

933 *Figure 13. Modeled temperature histories compared with temperatures estimated from clumped*
 934 *isotopes (modified after Mangenot et al., 2018). The black line represents the temperature/time*
 935 *path determined by $\Delta_{47}/U/Pb$ as proposed by Mangenot et al., (2018) while the dashed black line*
 936 *represents the modelled 1D thermal history for Ambreville well according to Uriarte (1997).*

937

(1 column)

938

939

940

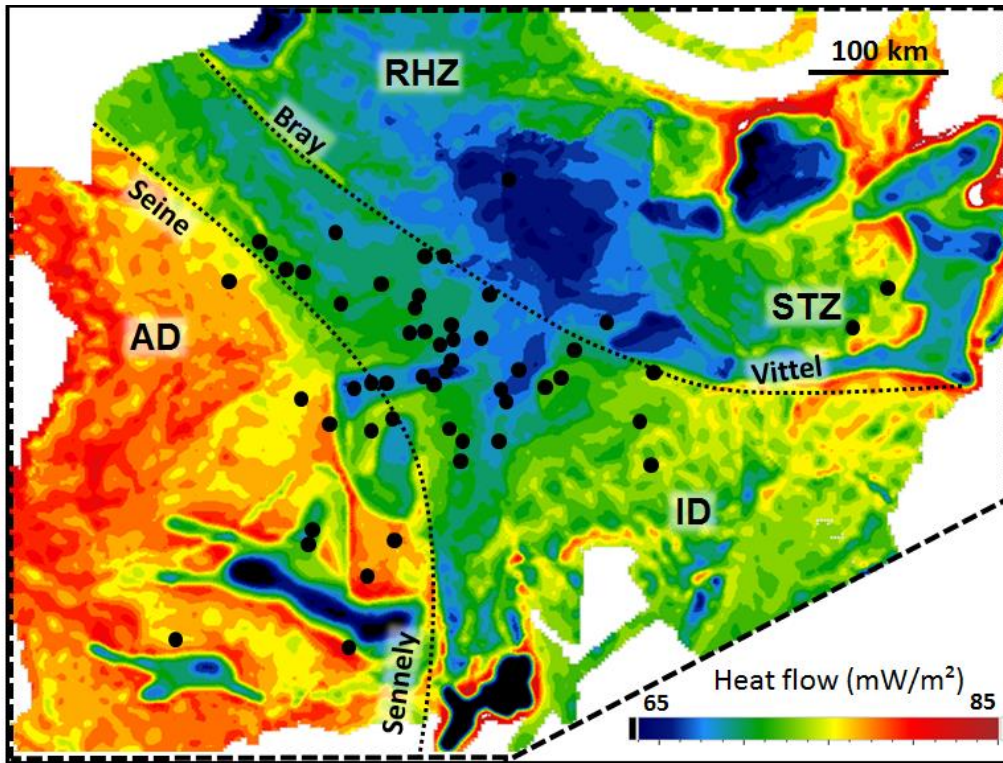
941

942

943

944

945



946

947 *Figure 14. Modelled present-day basal heat flow map (mW/m^2) of the Paris Basin. The distribution*
 948 *of heat flow highlights the effect of the crustal heterogeneities separated by the main deep faults*
 949 *defined in the model (dashed lines). The higher heat flow area (AD block) is in the western part,*
 950 *just above the more radiogenic crust. The effect of the sediment cover can also be seen in the*
 951 *central segment and in the Permo-Carboniferous basins where the sedimentary cover is thicker*
 952 *(RHZ/STZ blocks). The black dots show the distribution of the wells used to calibrate the thermal*
 953 *regime of the basin.*

954

(1 column)

955

956

957

958

959

960

961

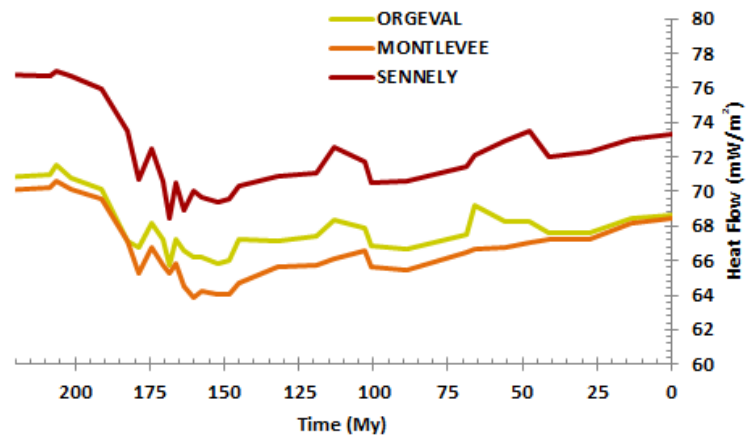
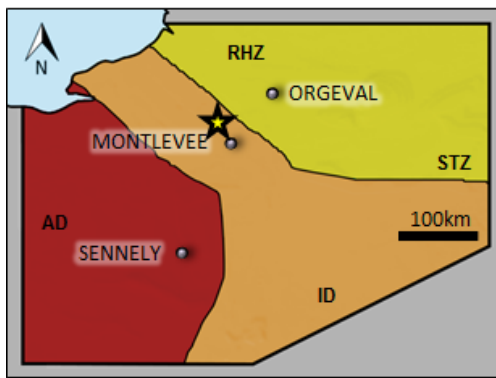
962

963

964

965

966
967
968
969
970
971
972

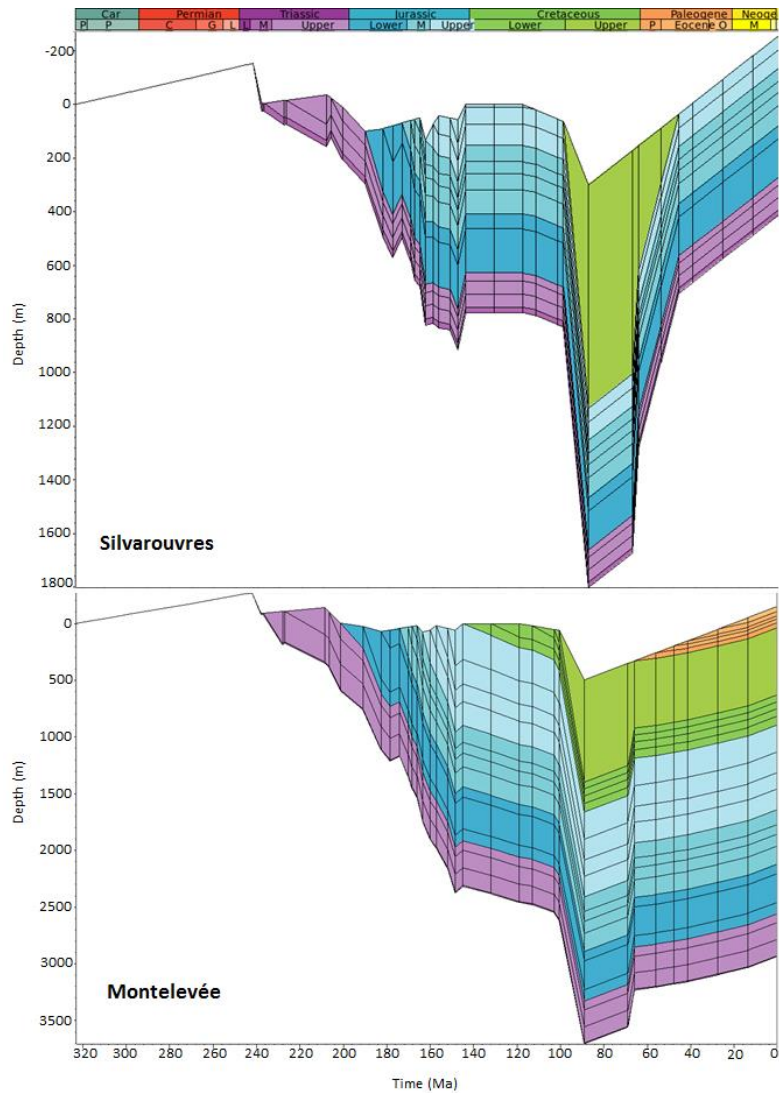


973
974
975
976
977
978
979
980
981
982
983
984
985
986
987
988

Figure 15. Modelled heat flow history of the Paris Basin for three wells located in the three different crustal domains (see Figure 1). The yellow star represents the location of Paris.

(2 column)

989
990
991
992
993
994



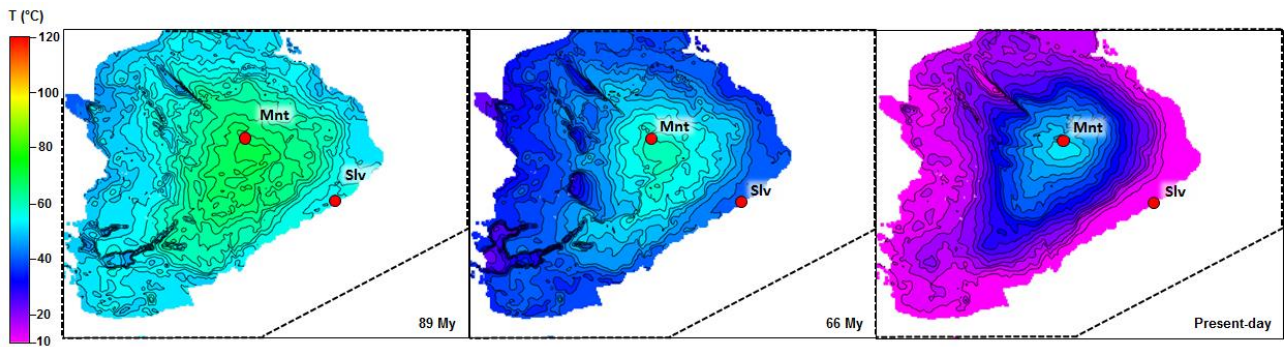
995

996 *Figure 16. Burial history of two wells located in different parts of the basin. The well positions are*
997 *shown along the cross-section in Figure 1 and Figure 9. The Silvarouvres well, located in the*
998 *eastern part of the basin, experienced a lower burial and a higher erosion of the chalk sediments*
999 *compared to Montelevée well, located in the central area.*

1000
1001
1002

(1 columns)

1003
1004
1005
1006
1007



1008

1009 *Figure 17. Modeled temperature distribution over time in the Dogger formation in Upper*
1010 *Cretaceous, end Cretaceous and present day, from left to right. The well position is shown along*
1011 *the cross-section in Figure 1 and Figure 9 (Mnt=Montelée well; Slv=Silvarouvres well).*

1012

(2 columns)

1013

1014

1015

1016

1017 *Table 1. Summary of the data used to build the 3D basin model.*

Top Age (Ma)	Layer Name	Erosion Phase	Deposition	Erosion	Deposition/ Erosion	Hiatus	Paleo- Bathymetry
0.0	Topography		✓				
13.7	Oligocene		✓				
27.5	Priabonian		✓				
41.3	Luthetian		✓				
47.8	Ypresian	Laramide			✓		
56.0	Paleocene	Laramide			✓		
66.0	Lower Paleocene	Laramide			✓		
69.0		Laramide		✓			✓
						✓	
89.0	Chalk		✓				
100.5	Gault Shale		✓				✓
103.0	Albian		✓				
113.0		Austrian		✓			
119.0	Aptian		✓				✓
132.0	Barremian		✓				
145.0		Neo-Cimmerian		✓			
148.5	Thitonian		✓				✓
152.0	Kimmeridgian		✓				✓
157.3	Oxfordian		✓				✓
160.0	Sequanian		✓				
163.5	Callovian		✓				✓
166.0	Bathonian		✓				✓
168.3	Upper-Bajocian		✓				
170.3	Lower-Bajocian		✓				✓
174.1		Mid-Cimmerian		✓			
178.4	Toarcian		✓				
182.7	Phliensbachian		✓				✓
191.0	Hettangian-Sinemurian		✓				✓
201.3	Rhetian		✓				✓
206.5		Upp Paleo-Cimmerian		✓			
208.5	Norian		✓				✓
227.0		Mid Paleo-Cimmerian		✓			
228.0	Carnian		✓				✓
237.0		Lower Paleo-Cimmerian		✓			
238.0	Ladinian		✓				✓
242.0	Anisian-Scythien		✓				✓
245.0	Red-Permian		✓				
272.0	Grey-Permian		✓				
298.0	Stephanian		✓				
309.0	Westphalian		✓				

1018

1019

1020 *Table 2. Thermal parameters of fully compacted (zero porosity) rock matrix used in thermal model.*

	Thermal Conductivity (W / m. °C)	Radiogenic Heat Production (μW/m ³)
Limestone	3.5	0.6
Dolostone	5.5	0.3
Chalk	3.2	0
Marl	1.9	1.3
Salt	6.1	0
Silt	2.5	1.2
Sandstone	6.8	0.5
Shale	2.3	1.9

1021

1022

1023

1024

1025

1026

1027

1028

1029

1030

1031

1032

1033

1034

1035

1036

1037

1038 *Table 3. Average thickness and average radiogenic heat production for the lower crust and the*
 1039 *three upper-crust domains (see Figure 1 for location).*

	UPPER CRUST		LOWER CRUST	
	Radiogenic Heat Production ($\mu\text{W}/\text{m}^3$)	Average Thickness (km)	Radiogenic Heat Production ($\mu\text{W}/\text{m}^3$)	Average Thickness (km)
ID	3.7	19	0.4	11
AD	4.0	26	0.4	16
RHT/STZ	3.4	22	0.4	13

1040